N000141812157 : Intracranial Waveguide, Resonance Cavity, and Cavitation Behavior

Reporting Period: JUN 16, 2019 to JUN 15, 2020

Date Received:

Submitter: Carey Balaban

Distribution Statement: Approved for public release; distribution is unlimited.

Major Goals

Objective 1. Develop and validate models for the waveguide, resonance cavity and acoustical cavitation properties of intracranial contents. Objective 2. Construct and validate advanced eye movement and pupil monitoring technology (VOG) for assessing warfighter readiness in operational environments. Deliverables: 1. Numerical models of intracranial contents, including blood flow, cavitation properties, and RF and acoustic absorption. A 1D model followed to a fully coupled, cavitating finite element analysis model. 2. Construct and test physical models to validate the RF and acoustic properties of the simulation models. 3. An improved VOG system embedded in a virtual reality display to increase the temporal bandwidth, refine algorithms and on-board processing capabilities for operational environments,

---

Accomplishments Under Goals

We have continued to refine initial numerical models of high frequency sound propagation in the human head, focusing on the temporal bone and inner ear, to explain perceptual phenomena of directed exposure to 40-70 kHz ultrasound sources. High-resolution finite element models have been constructed from digital image sets of human and macaque (M. fascicularis) heads for simulations that use ANSYS, COMSOL and MATLAB. The standard acoustics component of the analyses assesses transmission loss in Region I (low frequency regime, where transmission is controlled by stiffness and resonances), Region II (middle frequencies, where transmission loss increases with frequency and proportional to the structural mass) and Region III (higher frequency coincidences between sound wavelength(s) and structural wavelength(s) of the target objects yield enhanced transmission). The analyses suggest that there is a second conductive pathway for airborne, high frequency vibration to intracranial contents (see attached conference paper submission). It is well known the normal conductive hearing (audible range) depends upon the conduction of sound from to the inner ear via the pinna (ear lobe)-external ear canal, tympanic membrane (ear drum) and middle ear ossicles. However, sounds above the range of human hearing (ultrasound) can also be ‘heard’ when directed from behind a person at the mastoid process of the temporal bone. In humans and some primates, the mastoid is divided into air cells by thin septa of cortical bone (~0.2 mm thick), which are continuous with the middle ear air space and Eustachian tube. High resolution finite element models have been used to examine the acoustic properties of the bony and soft tissues of the human skull base, including the mastoid air cells, ossicles, inner ear, endolymphatic sac, tympanic membrane and brain. These analyses demonstrate significant, spatially localized resonance behavior, consistent with a hypothesis that the middle ear may have a previously unsuspected conductive pathway for high frequency pressure waves to the cochlea and vestibular system. Harmonic acoustic analysis and modal analyses of the mastoid and skull base support the likelihood of perceptual effects on hearing and balance. These findings raise the exciting possibility that there are two systems for directing sound to the ear. The traditional conductive path is a forward and laterally

directed system for detecting and localizing sound energy in the audible range. A second system appears to be sensitive to incident sound outside the normal audible range (>20 kHz), directed from behind the ear lobes at the mastoid region of the temporal bone. The mastoid region and skull base appear to be specialized for detecting and conducting energy to the endolymphatic sac and the vestibular apparatus of the inner ear. Exposures to unnatural, high frequency pressure fluctuations in this range would be expected to produce aberrant vestibular perceptions. We have been refining and testing numerical models of high frequency sound effects in the perilymph and endolymph-filled fluid spaces of the inner ear. Simulation tools include ANSYS, COMSOL and MATLAB. The models represent the inner ear as two fluid filled waveguide compartments, containing air-saturated fluids. The models incorporate physical properties of air bubble dynamics, including rectified diffusion and cavitation (including Schnerr-Sauer and Zwart-Gerber-Belamri models used in FLUENT). We have begun the implementation of these approaches to bubble dynamics in numerical simulations with geometrically complex models. Modal analyses of both human and cynomolgus monkey models identified the semicircular canals as the site of several acoustic resonant features. Features of the human model are described as follows. For a more detailed exposition, please see the uploaded draft conference paper for Proceedings of the ASME 2020 International Mechanical Engineering Congress and Exposition. Mode shapes of a so-called “open-open” half-wave acoustic resonator, were observed at 42.8 kHz (posterior semicircular canal) at 54.9 kHz (superior semicircular canal) and a higher-order mode at 77 kHz (posterior and superior semicircular canals near the crus commune). These ultrasonic resonance ‘windows’ correspond spatially to sites of ‘third window’ or semicircular canal dehiscence defects, which produce balance symptoms by permitting aberrant sound transmission into the vestibular apparatus. We have also incorporated particulate material in the endolymph of the vestibule into simulations (e.g., Kao et al. Laryngoscope, 127:709–714, 2017) to explore potential effects of high frequency sound on its dispersion and bubble dynamics. The disperion of this material in the semicircular canal ducts is a cause of symptoms in Benign Paroxysmal Positional Vertigo. Modal analysis of the middle ear cavity and mastoid air cells has revealed several resonances of interest. The first two natural frequencies (at 5.7 kHz and 13 kHz) are closed-closed “acoustic duct” modes along the long axis of the air space. The region also displayed higher-order modes at 27.5 kHz and 32.5 kHz at sites immediately adjacent to the semicircular canals. Another mode at 30.5 kHz, is perpendicular to the longitudinal mode shown a 5.7 kHz and is housed entirely within the mastoid air cells. Because the speed of sound differs markedly in air and water, dynamic changes in the air bubble distribution can profoundly affect the speed of sound (and hence energy distribution) along the cochlear waveguide. Because the sensory apparatus (organ of Corti) is embedded in a resonant basilar membrane, the changes in bubble distribution can affect both the perception of sound and patterns of mechanical injury in the inner ear from intense sound exposures. Our simulations suggest very profound effects on energy intensity near the base of the cochlea, with the expectation of high intensity energy delivery at the junction between the scala vestibuli and the vestibule. These studies are providing a basic understanding of mechanisms for potentially injurious effects of high frequency sound on the auditory and vestibular sensory apparatus. Specifically, we posit that an ultrasonic carrier signal with frequency near a major resonant feature can deliver sound directly to inner ear sense organs. The amplitude modulation process (“heterodyning”) comprises multiplication of two sinusoidal signals, typically known as an information signal and a higher-frequency carrier signal. The output signal contains energy at two new frequencies: the sum and difference of the original carrier and information signals. We are nearing completion of a prototype steerable ‘phased array’ speaker of piezoelectric emitters for delivering focused, amplitude modulated ultrasound (Pareto Optimal, Steerable Vogel’s Spiral Parametric Array at 40 kHz). The output beam is steerable over a 30 degree arc, controlled by an Intel/Altera Cyclone V FPGA. It will be tested in collaborative experiments at Army Research Laboratory after the post-COVID reopening. We have published a new peer-reviewed paper in Frontiers in Neurology: Neuro-Ophthalmology (open access journal) that documents an objective and non-invasive test to distinguish symptomatic individuals from an acute exposure in Havana

('UBI'), for individuals with an acute mild concussion and control individuals (nearly 90% correct 3-way classification). It is potentially forward-deployable with current technology (about 6.5 level) with an FDA approved device. We have completed testing and validation of a working prototype of a video-oculography system running at 1000 FPS on each eye. We intend to incorporate it in human subject studies after the end of the COVID closings of our laboratories. The footprint can be reduced for installation in most headgear, including diving and aviation helmets.

Plans Next Period

We will continue development of the simulations and devices. The 3D models will be refined for the skull base and soft tissues of the human and cynomolgus monkey. Cadaver measurements for model validation will be conducted in collaboration with Army Research Laboratory (ARL), though the PI's joint appointment as a Physical Scientist. Newly constructed small, steerable sound delivery devices will be tested for their ability to deliver envelope modulation of an ultrasonic carrier frequency in air and will be used in cadaver validation work with ARL. Predictions for testing stimulus efficacy from our simulations will be tested at ARL, where collaborative work will extend the simulation approaches to internal acoustic emissions from other directed energy sources, such at photoacoustic phenomena. Our modeling approaches and philosophies are very compatible and the tools/simulations are inter-operable. Work on the effects of electrical and magnetic directed energy on the intracranial contents, including the auditory and vestibular system, will continue to proceed collaboratively in order to optimize all our efforts. We have a strong sense that we (the extended team) are on the verge of some fundamental basic findings. We will conduct some 'proof-of-concept' experiments on physical models and cadaver materials, combining capabilities and resources to validate the simulations. Our publication of oculomotor criteria for distinguishing the symptomatic Havana individuals from controls and individuals with acute mild traumatic brain injury motivates technology development toward deployment. We will work with form factor reduction in a new oculomotor goggle prototype for higher speed, more sensitive video-oculography with an on-board FPGA. Prototype production has been discussed with the CTO of Neurolign Technologies, which purchased our previous partner, Neuro Kinetics, Inc. We will then have a prototype of field-deployable device for detecting some consequences of Havana-type energy exposures

---

Results Dissemination

In addition to standard professional forums, these findings are of special interest to directed energy researchers at ARL, where Dr. Balaban has a joint appointment as a Physical Scientist, and NRL (John O'Donnell). We have disseminated results in briefings. A recent publication in Frontiers in Neurology Neuro-Ophthalmology (an open journal) presents an objective, highly accurate clinical algorithm for differentiating individuals with Havana-type exposures from individuals with acute mild traumatic brain injury and control subjects (across a broad age range). A peer-reviewed conference paper will disseminate results of our numerical simulation studies at a major national mechanical engineering meeting (with specialized acoustics sessions).

Honors and Awards

Nothing to Report

Training Opportunities

The simulation studies have provided a continuous stream of technical challenges for model construction and software integration. The design and construction of the Pareto Optimal, Steerable Vogel's Spiral Parametric Array at 40 kHz and the associated phased-array control software for the

FPGA has also provided an opportunity to work through alternate engineering strategies. The greatest professional development, though, has been our mutual integration of knowledge in biological structure/anatomy, physiology, psychoacoustics, materials science, acoustical engineering, and applied physics. Our main weekly meetings commonly last for 2 hours and have become brainstorming sessions that generate new reading lists—and insights that drive the work forward.

Technology Transfer

The PI has a joint appointment as a Physical Scientist with WMRD at Army Research Laboratory. We share data and are collaborating in directed energy studies.

Participants

Name	Role	Person Months
Vipperman, Jeffrey	Co PD/PI	3
Klinzing, George	Co-Investigator	2
Dumm, Christopher	Graduate Student (research assistant)	6
Hiers, Anna	Graduate Student (research assistant)	6
Balaban, Carey	PD/PI	3

frontiers

Author's Proof

Carefully read the entire proof and mark all corrections in the appropriate place, using the Adobe Reader commenting tools (**Adobe Help**). We do not accept corrections in the form of edited manuscripts.

In order to ensure the timely publication of your article, please submit the corrections within 48 hours.
If you have any questions, contact neurology.production.office@frontiersin.org.

Quick Check-List

- **Author names** - Complete, accurate and consistent with your previous publications.
- **Affiliations** - Complete and accurate. Follow this style when applicable: Department, Institute, University, City, Country.
- **Tables** - Make sure our formatting style did not change the meaning/alignment of your Tables.
- **Figures** - Make sure we are using the latest versions.
- **Funding and Acknowledgments** - List all relevant funders and acknowledgments.
- **Conflict of Interest** - Ensure any relevant conflicts are declared.
- **Supplementary files** - Ensure the latest files are published and that no line numbers and tracked changes are visible. Also, the supplementary files should be cited in the article body text.
- **Queries** - Reply to all typesetters queries below.
- **Content** - Read all content carefully and ensure any necessary corrections are made.

Author Queries Form

Query No.	Details Required	Author's Response
Q1	Your article has been copyedited to ensure that we publish the highest quality work possible. Please check it carefully to make sure that it is correct and that the meaning was not lost during the process.	
Q2	The citation and surnames of all of the authors have been highlighted. Please check all of the names carefully and indicate if any are incorrect. Please note that this may affect the indexing of your article in repositories such as PubMed.	
Q3	Confirm that the email address in your correspondence section is accurate.	
Q4	If you decide to use previously published, copyrighted figures in your article, please keep in mind that it is your responsibility, as the author, to obtain the appropriate permissions and licenses and to follow any citation instructions requested by third-party rights holders. If obtaining the reproduction rights involves the payment of a fee, these charges are to be paid by the authors.	
Q5	Ensure that all the figures, tables and captions are correct, and that all figures are of the highest quality/resolution.	
Q6	Verify that all the equations and special characters are displayed correctly.	

Query No.	Details Required	Author's Response
Q7	Ensure to add all grant numbers and funding information, as after publication this is no longer possible.	
Q8	Ensure, if it applies to your study, the ethics statement is included in the article.	
Q9	Could you please confirm if all author affiliations are fine as listed?	
Q10	Please reduce short running title to maximum of five words.	
Q11	Please confirm whether the keywords are fine. Please keep the keywords list to a maximum of eight.	
Q12	Please confirm whether the heading levels in the article have been identified correctly.	
Q13	Please confirm that the Data Availability statement is accurate.	
Q14	Kindly confirm if the details appearing in the "Author Contributions" section are correct and make sure all authors listed in the Author's list are mentioned there.	
Q15	Please confirm if the text included as "Conflict of Interest" is fine. If not please provide the same.	
Q16	Please confirm whether the formatting of "Tables 1-4" is fine.	
Q17	Check your Appendix and confirm that it is correct.	
Q18	Please cite "Figure A1" inside the text.	
Q19	Please confirm whether the insertion of the Appendix citation is fine in lines 303 and 568.	

frontiers in Neurology

ORIGINAL RESEARCH
published: xx May 2020
doi: 10.3389/fneur.2020.00469

Distinctive Convergence Eye Movements in an Acquired Neurosensory Dysfunction

Carey D. Balaban[1,2,3,4]*, *Mikhaylo Szczupak*[5], *Alexander Kiderman*[6], *Bonnie E. Levin*[7] and *Michael E. Hoffer*[5,8]

[1] Department of Otolaryngology, University of Pittsburgh, Pittsburgh, PA, United States, [2] Department of Neurobiology, University of Pittsburgh, Pittsburgh, PA, United States, [3] Department of Communication Sciences & Disorders, University of Pittsburgh, Pittsburgh, PA, United States, [4] Department of Bioengineering, University of Pittsburgh, Pittsburgh, PA, United States, [5] Department of Otolaryngology, University of Miami Miller School of Medicine, Miami, FL, United States, [6] Neuro Kinetics, Inc., Pittsburgh, PA, United States, [7] Department of Neurology University of Miami Miller School of Medicine, Miami, FL, United States, [8] Department of Neurological Surgery, University of Miami Miller School of Medicine, Miami, FL, United States

In late 2016, diplomats in Havana, Cuba, began presenting with a unique symptom complex after perceiving a strange noise and/or feeling a pressure field in their domicile. This report is a retrospective, quantitative analysis of video-oculography data of pupillary light reflex performance and binocular disparity-driven eye and pupil movements during the acute time period after the reported exposure. The patterns of response in these 19 individuals are markedly different than those seen in a group of individuals with the usual acute mild traumatic brain injury (17 subjects) and from 62 control subjects (21–60 years old) with no injury. Non-linear least squares regression was used to estimate the model parameters from the eye movement and the pupil measurements (1). Linear discriminant analysis was then used to identify a classifier for an objective discrimination of the groups with >91% accuracy and no confusion between the acute neurosensory findings among the members of the Havana diplomatic community and the subjects with acute mild traumatic brain injury. This pattern difference in eye and pupil behavior may be a useful screen to help objectively distinguish blunt trauma from Havana-type effects in the future and to guide the affected individuals to appropriate care.

Keywords: vergence eye movements, pupil regulation, human, objective diagnosis, video-oculography

OPEN ACCESS

Edited by:
Aki Kawasaki,
Hôpital Ophtalmique
Jules-Gonin, Switzerland

Reviewed by:
Larry Allen Abel,
The University of Melbourne, Australia
Tara Alvarez,
New Jersey Institute of Technology,
United States

***Correspondence:**
Carey D. Balaban
cbalaban@pitt.edu

Specialty section:
This article was submitted to Neuro-Ophthalmology, a section of the journal Frontiers in Neurology

Received: *29 July 2019*
Accepted: *29 April 2020*
Published: *xx May 2020*

Citation:
Balaban CD, Szczupak M, Kiderman A, Levin BE and Hoffer ME (2020) Distinctive Convergence Eye Movements in an Acquired Neurosensory Dysfunction. Front. Neurol. 11:469. doi: 10.3389/fneur.2020.00469

INTRODUCTION

Complaints of sudden-onset tinnitus, ear pain, and dizziness emerged in late 2016 to early 2017 among diplomatic personnel and their families in Havana, Cuba. These affected individuals often reported hearing a loud, high-frequency, localized sound, and were under the impression that it could follow them in a room. Examinations and formal testing at the University of Miami in the acute to the subacute time frames found had objective evidence of both an otolithic abnormality and of cognitive dysfunction in a group of 25 individuals (2). When 21 exposed individuals were examined in a more chronic time frame (average of 201 days post-perception of exposure), 20 subjects reported persistent symptoms and signs that resembled the aspects of mild traumatic brain injury (3). As noted previously (2), their findings are not inconsistent with either a partially compensated vestibulopathy or a mild brain trauma (or both). When seen at the

University of Miami, these patients underwent diagnostic examinations that were guided by their symptoms and standard of care. As part of these examinations, all individuals underwent detailed video recordings of eye movements. These findings were reviewed, respectively, on an approved protocol (2) and formed the basis of the data set used in this study. The goal of this study was to provide a more detailed look at the eye motion seen in this patient group and compare these findings to other groups of individuals undergoing the same tests. The findings might allow investigators to begin to develop a set of objective findings that are typical for the acute neurosensory dysfunction among some members of the Havana diplomatic community.

The singular emergence of this cluster of individuals, the limited acute clinical information, the wide publicity about perceptions and symptoms, and the lack of etiologic information raise the practical issue of how one recognizes a similar presentation objectively in other individuals reporting the same perceptions. In the course of the acute examinations of the affected individuals from Havana, digital video records of eye movements were recorded for the qualitative assessment of pupillary light responses and vergence eye movements. These archival eye recording data have been analyzed retrospectively based upon algorithms from a recent publication that assessed both the vergence eye movements and the coordinated changes in pupil area during binocular disparity-driven convergence in more than 50 control subjects (1). Because convergence insufficiency (4–6) and pupillary light reflex effects (7) are described in the mild traumatic brain injury (mTBI) literature, detailed analyses are likely germane to the differential diagnosis of the Havana individuals. The patterns observed in this group of patients are compared with similar data from individuals with acute mTBI and our retrospective control group produced a discriminant function to differentiate among Havana affected, control, and acute mTBI samples. We hypothesize that the acute neurosensory presentation of these individuals will show features that are distinct from those of the standard acute mTBI.

MATERIALS AND METHODS

Participants and Study Design

The analysis of de-identified, retrospective data was approved by the University of Pittsburgh Institutional Review Board and the institutional review board (IRB) at the University of Miami and the Madigan Army Medical Center. The de-identified data were analyzed from three cohorts of subjects:

Control Subjects

A cohort of 64 normal subjects came from the University of Miami and the Madigan Army Medical Center. Fifty-two subjects are described in a previous communication (1), supplemented by 12 subjects to span the age range of the mTBI and Havana affected cohorts. They provided data with written informed consent under protocols approved by the IRBs at the University of Miami and the Madigan Army Medical Center and in accordance with the Declaration of Helsinki. The subjects were 42 males and 22 females, ranging from 21 to 60 years of age (mean 32.3 ± 10.0 years of age, SD).

Mild Traumatic Brain Injury Subjects

A cohort of 18 subjects from the University of Miami, the Naval Medical Center San Diego, and the Madigan Army Medical Center (17 with complete data) provided data with informed consent under protocols approved by the IRBs at the University of Miami, the Naval Medical Center San Diego, and the Madigan Army Medical Center and in accordance with the Declaration of Helsinki. The 14 male and four female subjects, ranging in age from 20 to 43 years (mean 29.1 ± 8.1 years of age, SD), were diagnosed as having mTBI by both an emergency room physician as well as one of the authors (MEH). The criteria used for the diagnosis included a standard military definition of having a head injury, suffering an alteration or loss of consciousness, and having new neurosensory symptoms with onset at the time of injury and persisting until during our team's evaluation (all individuals ended up to have symptoms for at least 1 week). In addition, these individuals could not have been diagnosed with more than mild brain injury [e.g., no loss of consciousness (LOC) or LOC <30 min, no subdural hematoma, no need for admission to the intensive care unit, and a Glasgow Coma Score of 14 or above]. All individuals were evaluated in the acute period [tested 58 ± 36 h (SD) after injury]. In addition, these individuals had no significant medical issues, no history of ear disease or ear surgery, no history of developmental learning issues, and no history of concussion for at least 1 year, with no lingering sequelae before the current injury.

Havana Affected Subjects

There were 19 subjects with complete vergence and pupil test data among the 25 affected subjects described in Hoffer et al. (2). The entire cohort was composed of 15 males and 10 females (mean 43.2 ± 12.6 years of age, SD; all under 64 years of age). There were 23 subjects with pupillary light reflex tests (mean age 42.0 ± 7.6 years, SD) and 19 subjects who also had both binocular step and smooth pursuit vergence tests (mean age 40.5 ± 9.1 years, SD; under 56 years of age). The analysis of de-identified clinical video-oculographic data was approved by institutional review board of the University of Miami and the University of Pittsburgh, respectively.

Pupillary Light Response and Binocular Disparity Vergence

Pupillary light responses and binocular disparity vergence eye movement performance were tested quantitatively with a clinical eye tracking system within a portable 3D head-mounted display system (I—PAS™; I-Portal® Portable Assessment System, Neuro Kinetics, Inc., Pittsburgh, PA, USA). Each eye views an independent circular portion of a 1,920 × 1,080-pixel stimulus display that subtends a 60° diagonal field of view. The subjects can adjust the focus of the video image for each eye across a ±4 diopter range. Video-based eye tracking is performed under continuous 940-nm infrared illumination at a sampling rate of 100 Hz. The pupils are identified by characteristic luminance boundaries. The pupil area is measured from each image at a resolution of 139 pixels/mm^2. The instantaneous eye position is calculated from the centroid of the identified pupil area over a horizontal range of ±30° and a vertical range of ±20°.

Neuro Kinetics VEST™ software was used for testing and data collection. All stimuli were rendered in the virtual environment that was created by the enclosed video display, with synchronization of the stimulus refresh rates and the eye tracking sampling rate. Eye movement recordings were calibrated for a series of conjugate horizontal and vertical gaze shifts using spot targets subtending ∼0.1° of the visual angle. Vergence angle is represented in degrees relative to zero at initial fixation. Normal consensual pupil responses were confirmed during the neurological examination. For testing the pupillary light reflex quantitatively, the subjects viewed binocularly a 5° (visual angle) disc centered on the visible area of each screen half while 13 homogeneous illumination flashes (0.42 to 65.4 cd/m², 0.300 s on, 2.00–4.00 s off) were presented binocularly in an ascending order of intensity (**Figure 2**). Because the light-evoked and the vergence-related pupil movements were symmetric, the average area of the left and the right pupils was used in the final analyses.

Targets for the disparity fusion ("vergence tracking") task were a white square with a red center that subtended ∼0.1° of the visual angle for each eye. The total field luminance during the presentation of the square, measured with a spot luminance detector incorporating a LDM-9901 sensor (Gigahertz-Optik, Germany), ranged from 0.05 to 0.06 cd/m². The vergence disparity step task began with the illuminated targets at a central fixation position for each eye. The targets were then shifted at 4-s intervals between a disparity requiring 1.5° convergence (from the initial fixation target) and a disparity requiring 1.5° divergence (from the initial fixation target) in order to achieve binocular fusion. Five cycles of alternating convergence and divergence were presented over a 40-s duration (**Figure 3**, right traces). By convention, convergence is represented as a positive vergence angle. For the vergence pursuit (tracking) task, the trial began with the illumination of the two monocular targets at the initial focal point phoria (equivalent to ∼1 m in virtual depth). The target then moved smoothly through three cycles of a sinusoidal profile, such that the monocular targets moved simultaneously laterally and then medially to produce binocular disparity (i.e., the left eye target moved leftward, while the right eye target moved rightward, and then the left eye target moved rightward, while the right eye target moved leftward) with a cycle duration of 10 s (**Figure 3**, left traces). During this sinusoidal movement, the maximum deviation of the response from the initial position was ±2.6° of the visual angle in the horizontal plane.

Data Analysis

In addition to the analysis of raw pupil area data, the pupillary light response range was used to normalize the pupil area for analysis of coordinated eye and pupil movements during the vergence tasks. For those analyses, the maximum (A_{max}) and the minimum (A_{min}) pupil areas were determined separately for the left and the right eyes for responses on the range of low-intensity (0.42 cd/m²) to high-intensity (65.4 cd/m²) stimuli. The range-normalized area (1) was calculated from raw data for an additional set of analyses .

The pupil data were analyzed both as peak constriction velocity for each flash intensity and from the parameter estimation for a model described in the **Appendix**. For the former observation, the pupil velocity was calculated from the pupil area data (in mm²) with a "fitted slope" method, which fits a straight line between points from i–n : i + n (n = half-width of a user-specified window. The numerator for the slope calculation is the sum (points multiplied by offset), where offset is the range from –n to n, while the denominator is $n\,(n+1)\,(2n+1)/3$. The product of the slope and the sampling frequency yields the velocity. The half-width of the window was five points (50 ms) at a sample rate of 100 Hz.

The eye movements in the disparity step and the pursuit tasks were modeled as the weighted sum of first-order high- and low-pass representations of the vergence target position with a processing delay (1). The general architecture of this simple model is diagrammed in **Figure 1**. Data fits by this model to the vergence eye movement of control subjects had high average coefficients of determination, which were 0.82 ± 0.04 for the step disparity task and 0.91 ± 0.02 for the pursuit disparity task. They are used as an adequate parsimonious model, with fewer free parameters for estimation than the more elaborate models such as that of Maxwell et al. (9).

Non-linear least squares regression ("lsqnonlin.m" function in MATLAB) was used to estimate the parameters for the

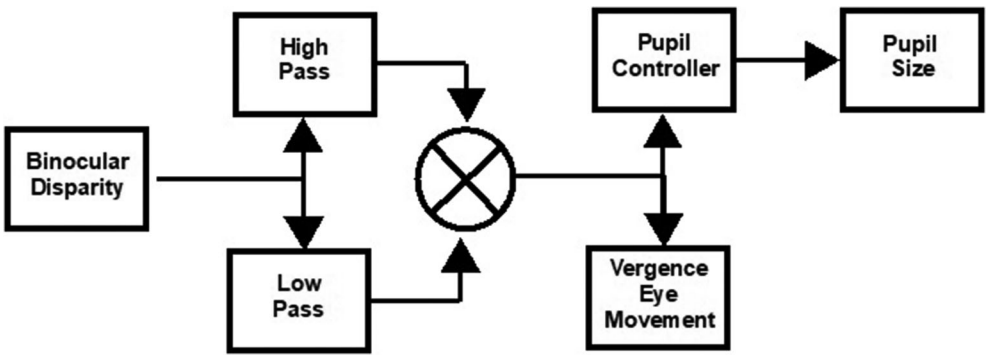

FIGURE 1 | Schematic of approach for model estimation of binocular disparity-driven vergence eye movement and pupil responses (1). The transfer functions are described in the text. The pupil controller Laplace form was adopted from Sun et al. (8) as a parsimonious descriptor of the data.

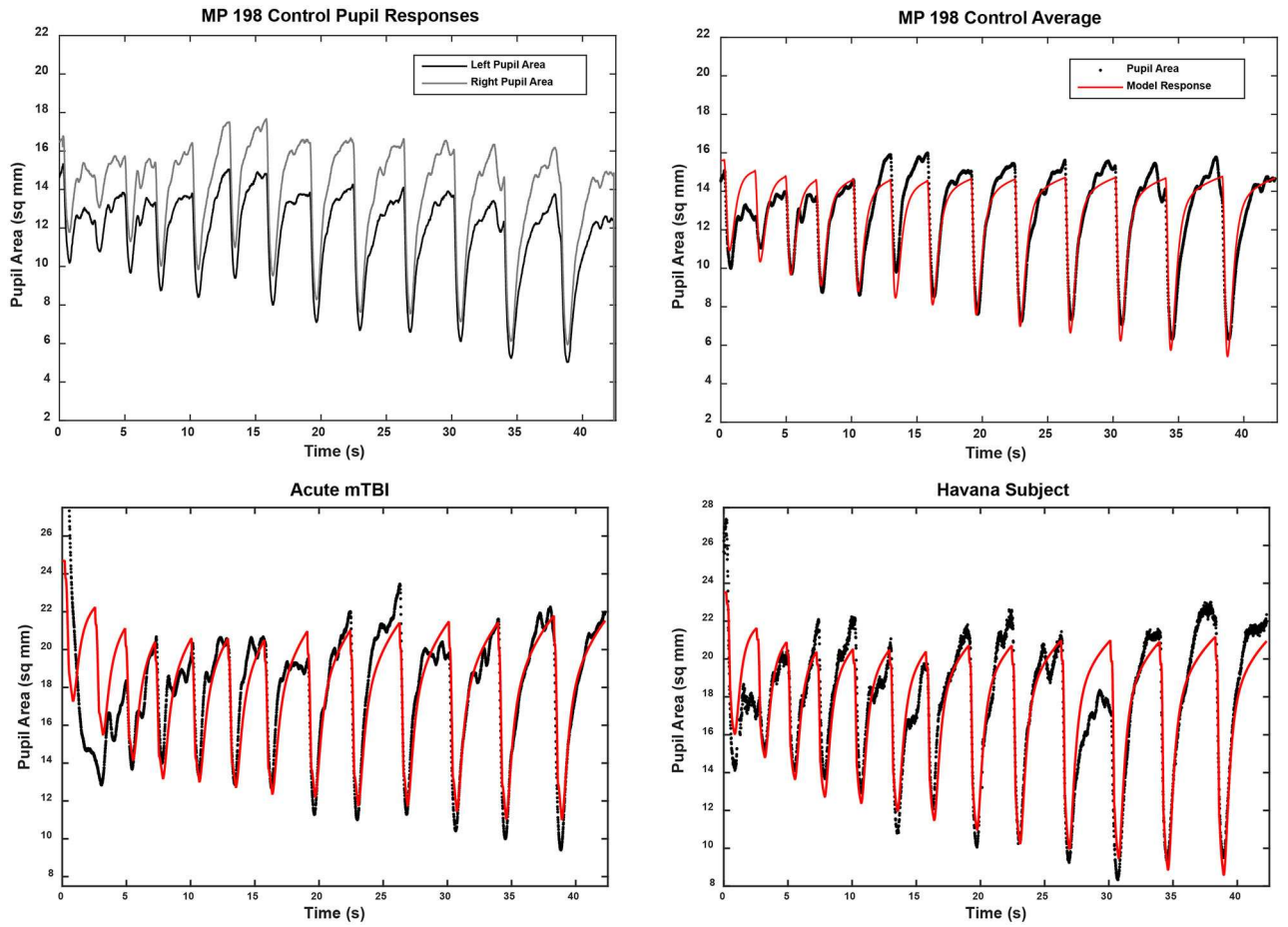

FIGURE 2 | Pupil area responses during binocular presentation of 13 homogeneous illumination flashes (0.42 to 65.4 cd/m², 0.310 s on, 2.03 s off). The upper left panel shows the parallel and the highly coherent responses of each eye from a control subject. In the other panels, the black traces show the average of the responses of both eyes from three subjects (one from each subject group). The modeled response for each trace is shown in red based upon the approach described in the supplemental material. Note the strong similarity in the dynamic responses across groups, which was confirmed by the lack of differences between the response parameters in quantitative analyses (see text).

vergence disparity response as a weighted sum of high-pass ($\frac{K_{vh}se^{-t_v s}}{s+1}$) and low-pass ($\frac{K_{vl}e^{-t_v s}}{0.25s+1}$) processes, with delay t_v and gains K_{vh} (phasic process) and K_{vl} (tonic process), respectively. The delay parameter accounts for the reaction time to the binocular disparity step stimulus; it was set at zero for the binocular disparity pursuit task. Based upon Sun et al. (8), the pupil controller dynamics were fitted from the vergence data by a transfer function for pupil motion, $\frac{K_p e^{-t_p s}}{0.28s+1}$, with delay t_p and gain K_p, which estimates the near response sensitivity directly. As shown in our previous publication (1), the residuals from this approach showed no activity in the range of the vergence eye movements, which indicates the descriptive adequacy of this simple model for the present analyses. The symmetry of the convergence responses was tested by fitting separate gains for convergence vs. divergence and for pupil constriction vs. dilatation.

Statistical analyses were performed in SPSS version 24 (IBM Corporation, Armonk, NY, USA). Kolmogorov–Smirnov tests (Lilliefors correction) were used to test the assumption of a Gaussian distribution for each dependent variable and group. For variables that were not rejected as Gaussian, paired comparisons between group data were performed by analysis of variance, followed by Tukey's highest significant difference (HSD) and Games–Howell *post hoc* tests. When the Gaussian assumption was rejected ($p < 0.05$), a distribution-free Kruskal–Wallis approach in the SPSS Non-parametric tests→Independent Samples menu was used. Stepwise discriminant analysis for the control, acute mTBI, and Havana affected subjects was performed on the parameters describing vergence eye and pupil movements, with a Wilks-lambda criterion and a one-out validation.

RESULTS

The pupillary light response to a series of binocular light flashes is shown in **Figure 2**. All of the subjects displayed

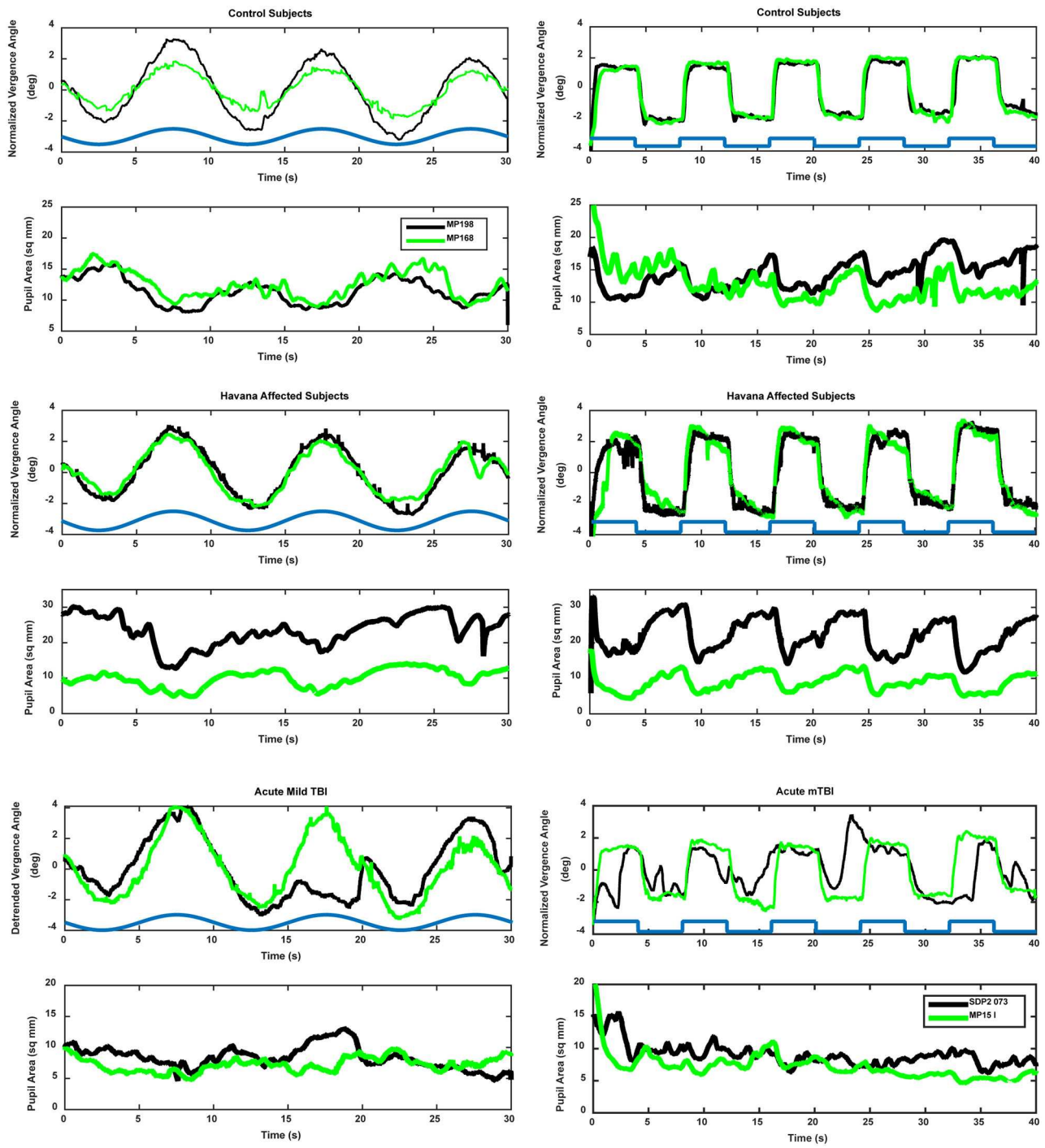

FIGURE 3 | Examples of vergence (upper trace, convergence in the positive direction) and concurrent pupil area changes (lower trace, area in mm^2) in control (upper panels), Havana affected (middle panels), and acute mild traumatic brain injury (lower panels). The time course of the retinal disparity stimulus is shown by the heavy blue line in the convergence panels, offset above the responses for illustrative purposes. Two different subjects (black and green traces) are shown for each group. The left panels show the responses during the binocular disparity pursuit task. The responses during the binocular disparity step task are shown on the right.

parallel right and left pupil size traces, which is illustrated for one control subject in the upper left panel (**Figure 2**). Hence, given the high coherence between the pupils, the main analyses were conducted on their averaged area. Note that a lumped parameter dynamic model (described in **Appendix**), based upon a series of published model iterations from the Stark laboratory

TABLE 1 | Parameter estimates for pupil light responses in the three groups of subjects (see text for details).

	Control group	Acute mild traumatic brain injury (mTBI)	Havana affected	Tukey's highest significant difference or Kruskal–Wallis ($p < 0.05$) comparisons	Least significant difference ($p < 0.05$) comparisons
Unadjusted measures					
Light reflex average baseline pupil area (mm^2)	18.24 ± 0.83 mm^2 (Gaussian)	16.46 ± 1.65 mm^2 (Gaussian)	14.15 ± 1.37 mm^2 (Gaussian)	C > HA; C = mTBI; HA = mTBI	
Light response fit to model (R^2, coefficient of determination)	0.68 ± 0.02 (Gaussian rejected)	0.56 ± 0.04 (Gaussian)	0.74 ± 0.03 (Gaussian)	C = mTBI; C = HA; HA > mTBI	
Age-adjusted measures for average pupil area in each task with significant age relationship (basis age: 33.3939 years)					
Light reflex average baseline pupil area (mm^2)	17.92 ± 0.78 mm^2	14.62 ± 1.53 mm^2	16.37 ± 1.50 mm^2		NS for all
Disparity step average pupil area (mm^2)	19.38 ± 0.83 mm^2	14.51 ± 1.64 mm^2	16.22 ± 1.62 mm^2		C = HA; C > mTBI; HA = mTBI
Disparity pursuit average pupil area (mm^2)	17.29 ± 0.84 mm^2	13.62 ± 1.66 mm^2	15.25 ± 1.64 mm^2		C = HA; C > mTBI; HA = mTBI

(8, 10–13), provided a reasonably robust fit to the responses in control, acute mTBI, and Havana affected subjects. There were no significant group differences in any parameter of dynamic behavior. However, two significant differences emerged in parameters between groups (**Table 1**). First, the average pupil area was significantly smaller in the Havana affected group than that of the control subjects, with an intermediate baseline pupil area in the acute mTBI subjects. Because there is a significant negative linear relationship between the average baseline pupil area and age in the control subjects (area $= -0.342$ * age $+ 29.176$, $r = -0.499$, $p < 0.001$), the analysis was repeated with age as a covariate, which eliminated significant group differences (**Table 1**). Second, the goodness of fit was significantly higher (mean $R^2 > 0.68$) for both the control and the Havana affected individuals than in the acute mTBI group (mean $R^2 = 0.55$). The goodness of fit was uncorrelated with age. A reduction in static pupil size in the affected Havana subjects during the light reflex testing was also observed for the average pupil area during the disparity step (control: 19.77 ± 0.92 mm^2, mTBI: 16.14 ± 1.72 mm^2, Havana affected: 13.35 ± 1.67 mm^2; $p < 0.01$ vs. control, Kruskal–Wallis test) and the disparity pursuit (control: 17.63 ± 0.91 mm^2, mTBI: 15.26 ± 1.70 mm^2, Havana affected: 12.66 ± 1.65 mm^2; $p < 0.05$ vs. control, Kruskal–Wallis test) responses. Because there are significant negative linear relationships between these measures and age in the control subjects, the analyses were repeated with age as a covariate (**Table 1**). The correction for age indicated that only the mTBI subjects had smaller average pupil areas than those of the controls.

For the analyses of the peak constriction velocity data (a measure of dynamic performance), the only significant effect was noted at one flash intensity (47.8 cd/mm^2). For that stimulus, the response was reduced significantly in the acute mTBI group relative to the control group (HSD test, $p < 0.05$, with the Havana exposed subjects not differing from either group).

Binocular disparity-driven tests provide a way to assess the coordination of movements related to convergence eye movements (1). Two test paradigms involve the presentation of small target spots to each eye to evoke convergent or divergent eye movements by moving toward the nose or away from the nose. For the disparity pursuit task, the targets move gradually to produce coordinated, sinusoidal convergence eye movements and changes in pupil area (**Figure 3**, left panels). Hence, it tests a low-frequency response. For the disparity step test (**Figure 3**, right panels), the targets move abruptly. It is included to examine the response at higher frequencies. In normal subjects, the dominant pattern of coordination is termed "near response": pupil constriction (decreased pupil area) during convergence and pupil dilation (increased pupil area) during divergence. The behavior of normal subjects and the methods of analysis are described in detail in a recent publication (1). Examples of the fidelity of the fit of the model analysis to the pupil data (from the vergence eye movements) are shown in **Figure 4** for one subject from the Havana affected group.

Disparity Step Task: Vergence Eye Movements

The binocular disparity step response test revealed several differences between the control, acute mTBI, and Havana affected subject groups. The traces in **Figure 3** show sharp, well-demarcated "square wave" vergence eye movement responses in the control and Havana affected groups, accompanied by robust pupillary responses. The eye movement and the pupil responses were attenuated and less sharply demarcated in the acute mTBI group.

The analysis of the responses (**Table 2**) showed that the acute mTBI group had significantly lower gains for the low-pass components of the eye movements than either

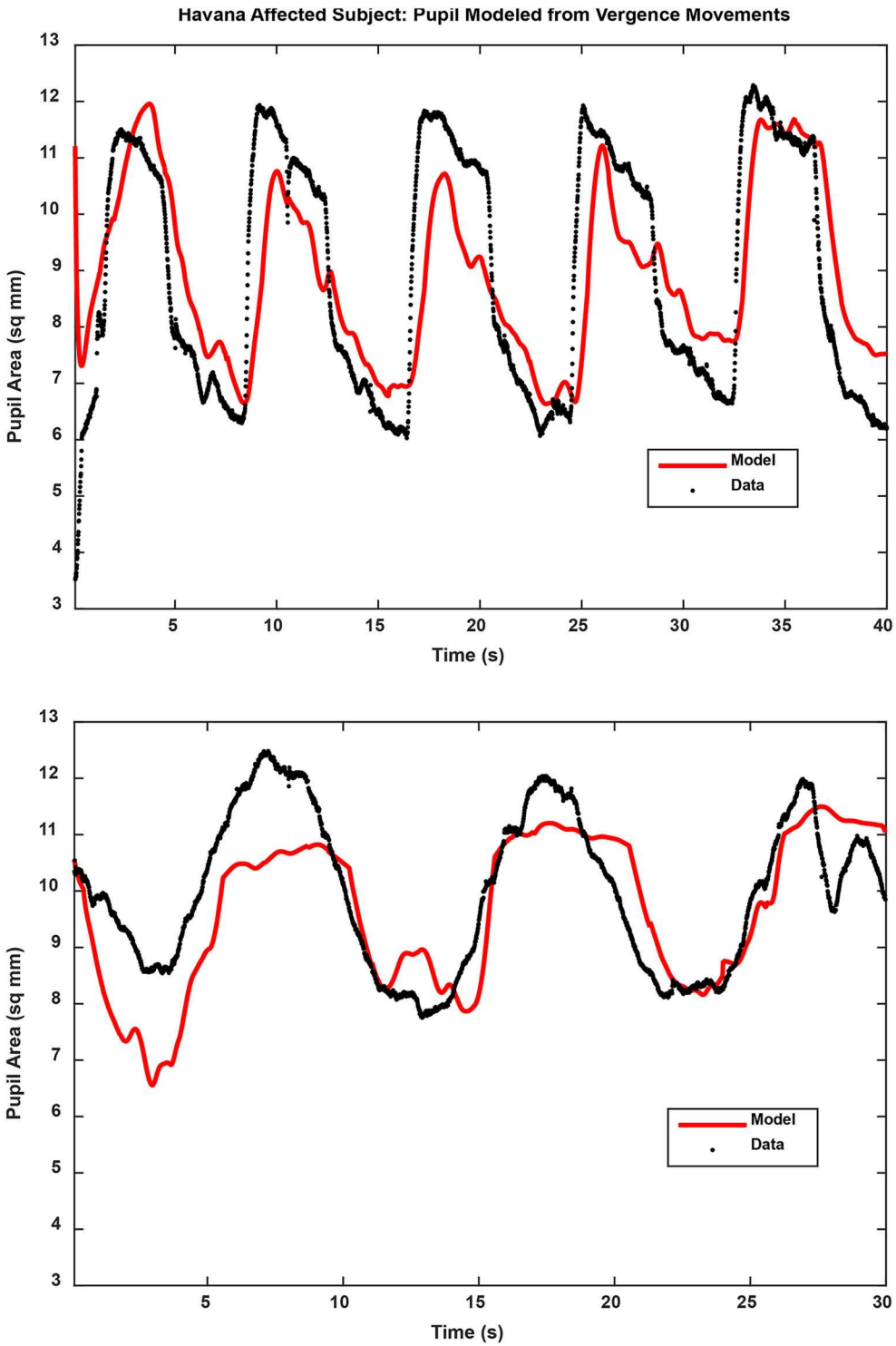

FIGURE 4 | Pupil traces (black) are shown for the binocular disparity step response (upper panel) and binocular disparity pursuit response (lower panel) from a Havana affected subject. The model fit, based upon the eye movement vergence response, is shown for each trace in red. The full results of the analyses are described in the text.

the control or the Havana affected subjects (Kruskal–Wallis tests, $p < 0.01$) as well as a significantly poorer goodness of fit (HSD tests, $p < 0.01$). By contrast, the disparity step-driven eye movements in the Havana affected subjects did not differ significantly from those of the control subjects.

Q16

TABLE 2 | Significant group differences in model parameter values for the disparity step responses.

	Control group	Acute mild traumatic brain injury (mTBI)	Havana affected	Tukey's highest significant difference or Kruskal–Wallis ($p < 0.05$) comparisons
Low pass convergence eye movement modulation depth (K_{vl} converge direction)	1.43 ± 0.09° (Gaussian rejected)	0.59 ± 0.17° (Gaussian rejected)	1.42 ± 0.16° (Gaussian rejected)	C > mTBI; C = HA; HA > mTBI
Low pass divergence eye movement modulation depth (K_{vl} diverge direction)	1.51 ± 0.08° (Gaussian rejected)	0.65 ± 0.16° (Gaussian rejected)	1.38 ± 0.15° (Gaussian rejected)	C > mTBI; C = HA; HA > mTBI
Vergence R^2	0.82 ± 0.04 (Gaussian rejected)	0.48 ± 0.07 (Gaussian rejected)	0.67 ± 0.07 (Gaussian rejected)	C > mTBI; C = HA; HA = mTBI ($p = 0.05$)
Pupil delay re: vergence in ° (s) [re: % light response range per degree vergence]	0.16 ± 0.02 s (Gaussian rejected)	0.13 ± 0.04 s (Gaussian rejected)	0.01 ± 0.04 s (Gaussian rejected)	C = mTBI; HA < C; HA = mTBI
	[0.07 ± 0.02] (Gaussian rejected)	[0.09 ± 0.04] (Gaussian rejected)	[−0.08 ± 0.04] (Gaussian rejected)	[C = mTBI; HA < C; HA < mTBI]
Pupil constriction sensitivity in $mm^2/°$ (re: vergence)	2.10 ± 0.22 $mm^2/°$ (Gaussian)	0.76 ± 0.41 $mm^2/°$ (Gaussian rejected)	1.89 ± 0.38 $mm^2/°$ (Gaussian)	C > mTBI; HA = C; HA = mTBI
[% light response range per degree vergence]	[7.5 ± 1.0%/°] (Gaussian)	[5.3 ± 1.9%/°] (Gaussian)	[16.7 ± 1.8%/°] (Gaussian rejected)	[C = mTBI; HA > C; HA > mTBI]
Pupil (re: vergence) R^2	0.47 ± 0.03 (Gaussian)	0.32 ± 0.05 (Gaussian)	0.55 ± 0.05 (Gaussian)	C = mTBI; HA = C; HA > mTBI

Q16

TABLE 3 | Significant group differences in model parameter values for the disparity pursuit responses.

	Control group	Acute mild traumatic brain injury (mTBI)	Havana affected	Tukey's highest significant difference or Kruskal–Wallis ($p < 0.05$) comparisons
Low pass convergence modulation depth (K_{vl} converge direction)	2.32 ± 0.10° (Gaussian)	1.71 ± 0.18° (Gaussian)	1.84± 0.16° (Gaussian rejected)	C > mTBI; C > HA; HA = mTBI
Low pass divergence modulation depth (K_{vl} diverge direction)	2. 25 ± 0.09° (Gaussian)	1.75 ± 0.16° (Gaussian rejected)	1.87 ± 0.14° (Gaussian rejected)	C > mTBI; C = HA; HA = mTBI
Vergence R^2	0.91 ± 0.02 (Gaussian rejected)	0.58 ± 0.04 (Gaussian rejected)	0.91 ± 0.04 (Gaussian rejected)	C > mTBI; C = HA; HA > mTBI
Pupil constriction gain in $mm^2/°$ (re: vergence)	1.67 ± 0.14 $mm^2/°$ (Gaussian rejected)	1.68 ± 0.217 $mm^2/°$ (Gaussian rejected)	1.46 ± 0.23 $mm^2/°$ (Gaussian)	NS in $mm^2/°$
[% light response range/° vergence]	[7.4 ± 0.6%/°] (Gaussian rejected)	[5.9 ± 1.2%/°] (Gaussian rejected)	[11.8 ± 1.0%/°] (Gaussian)	[C = mTBI; HA > C; HA > mTBI]
Pupil dilation gain in $mm^2/°$ (re: vergence)	0.42 ± 0.14 $mm^2/°$ (Gaussian)	−0.61 ± 0.26 $mm^2/°$ (Gaussian rejected)	0.56 ± 0.22 $mm^2/°$ (Gaussian)	C > mTBI; C < HA; HA > mTBI
[% light response range/° vergence]	[8.3 ± 0.9%/°] (Gaussian rejected)	[7.2 ± 1.7%/°] (Gaussian)	[6.5 ± 1.5%/°] (Gaussian)	NS in %PLR/°
Pupil (re: vergence) R^2	0.50 ± 0.02 (Gaussian)	0.30 ± 0.04 (Gaussian)	0.54 ± 0.03 (Gaussian)	C > mTBI; C = HA; HA > mTBI

Disparity Step Task: Dynamic Pupil Responses

A different picture emerged from the analyses of the dynamic pupil responses during the disparity step task. These movements are modeled as a parallel response to the signal generating the vergence eye movements [e.g., Balaban et al. (1)]. Separate analyses expressed the magnitude of the pupil response during disparity-driven vergence as either (1) pupil area per degree vergence ($mm^2/°$) or (2) pupil area as a normalized percentage of light reflex range per degree vergence. **Figure 3** (right panels) shows the distinct coordinated response of the pupil during the step vergence eye movements in two control and two Havana affected subjects and the much less distinct pupil responses in two subjects from the acute mTBI group. The reduced pupil coupling to the vergence eye movements in the latter group was apparent from the R^2 values for the model fits, which indicated that the eye movement component explained an average of 47% of pupil variability in the control subjects and 55% of the variability in Havana affected subjects, but only 32% of the variance (HSD test, $p > 0.01$ re: either group) in the acute mTBI subjects.

Figure 4 shows the examples of model performance for a representative Havana affected subject. The Havana affected

Q16

TABLE 4 | Discriminant function for control, acute traumatic brain injury (mTBI), and Havana affected patients from binocular disparity tests.

	Control (predicted)	mTBI (predicted)	Havana affected (predicted)
Classification results (one-out in square brackets)			
Control	61 [56]	1 [2]	0 [4]
mTBI	4 [6]	13 [11]	0 [0]
Havana affected	3 [6]	0 [0]	16 [13]
	1	**2**	
Standardized canonical discriminant function coefficients			
Vergence step modulation low-pass gain, converging direction	0.455	−0.651	
Vergence step modulation low-pass gain, diverging direction	0.674	0.320	
R^2 for vergence step modulation	−0.764	0.495	
Pupil (re: vergence) step modulation in $mm^2/^\circ$, converging direction	−0.053	1.003	
Pupil (re: vergence) step modulation in $mm^2/^\circ$, diverging direction	0.142	−0.280	
R^2 for pupil (re: vergence) step modulation	−0.178	0.215	
Pupil (re: vergence) step delay in % pupil range/°	−0.292	0.256	
Pupil (re: vergence) step gain, constriction direction in % pupil range/°	0.365	−0.835	
Mean pupil area (in mm^2) for vergence step	0.149	1.430	
Vergence pursuit modulation low-pass gain, converging direction	0.079	0.275	
Vergence pursuit modulation low-pass gain, diverging direction	−0.580	−0.277	
R^2 for vergence pursuit modulation	1.044	0.629	
Pupil gain (re: vergence pursuit), constriction direction in % pupil range/°	0.440	−0.193	
Pupil gain (re: vergence pursuit), dilation direction in % pupil range/°	0.096	0.596	
Mean pupil area during vergence pursuit (in mm^2)	−0.162	−0.441	
Pupil area in mm^2 (initial 200 ms of light response test)	0.165	−0.799	
R^2 for model fit to pupillary light reflex test	0.415	−0.155	
Mean pupil baseline between flashes in pupillary light test (in mm^2)	−0.237	−0.438	
Maximum pupil constriction velocity during pupillary light test	−0.299	−0.084	

Stepwise discriminant analysis, Wilks–lambda criterion, Vergence test data only; the cross-validated estimates are in brackets. The raw data analyses were 91.8% correct overall; 81.6% correctly classified in one-out cross-validation. The three-way separation with age-adjusted data (based on a control sample regression relationship to a standard age of 33.3939 years) was very similar, 89.8% correct overall, with no cross-classification errors between the mTBI and the Havana affected groups.

subjects showed a shorter estimated pupil response delay than the control group for $mm^2/^\circ$ data (HSD test, $p < 0.05$; marginal for comparison with the mTBI group) and the mTBI group for data normalized to the pupil light response (HSD test, $p < 0.05$; marginal for comparison with the control group). The pupil area modulation of the Havana affected subjects, measured in $mm^2/^\circ$, did not differ from that of the control for either constriction or dilation. In the acute mTBI group though, these responses were altered significantly with rectification of the response in the dilation direction. Finally, for data expressed as % pupil range, the Havana affected subjects had more robust pupil constriction responses than either the control or the acute mTBI group (Kruskal–Wallis tests, $p < 0.01$). The response sensitivity in the acute mTBI group did not differ from that of the control subjects.

Disparity Pursuit Task: Vergence Eye Movements

The binocular disparity pursuit task tests the disparity vergence performance over a slow, smooth pursuit cycle of 10 s. The traces in **Figure 3** (left traces) show smooth, sinusoidal vergence eye movement tracking responses in the control and the Havana affected groups, with coordinated pupillary responses that display a clear sinusoidal component. The eye movement and the pupil responses were small and less distinct in the acute mTBI group.

The analyses of the disparity pursuit task data (**Table 3**) revealed reduced vergence eye movement modulation (low pass) in the acute mTBI group (Kruskal–Wallis test, $p < 0.01$) relative to that of the control group, with the Havana affected group showing a reduction so that it differed from neither the control subjects nor the acute mTBI subjects. As in the case of the disparity step task, the goodness of fit (R^2) for vergence eye movements (to the stimulus profile) showed no difference between the control and the Havana affected subjects. Moreover, as in the case of the binocular disparity step task, the goodness of fit of the vergence eye movements of the acute mTBI subjects to the stimulus profile was reduced relative to those of both the control and Havana affected subjects (HSD tests, $p < 0.01$). These findings suggest that there is an impairment of the fidelity of disparity-driven vergence pursuit eye movement control in the acute mTBI subjects, but not in the Havana affected subjects.

Disparity Pursuit Task: Dynamic Pupil Responses

As mentioned previously regarding **Figure 3**, the subject groups differed in the appearance of the components of the pupil area responses that were related to the vergence eye movements. The R^2 values indicate that the eye movement component explained at least 50% of pupil variability in the control and the Havana affected groups, but only 32% of the variance (HSD test, $p > 0.01$ re: either group) in the acute mTBI subjects. The pupil area response (re: vergence eye movements) for constriction during the disparity pursuit task did not differ between groups when expressed as $mm^2/^\circ$ (**Table 3**). However, when pupil area was normalized as a percentile of the pupil response range, the Havana affected subjects had significantly higher sensitivity per degree of eye movement than either the control or the acute mTBI subjects. The coordinated pupil response sensitivities (pupil area re: vergence angle) did not differ between the step and the pursuit tasks for any groups.

Objective Classification of Subject Groups From Vergence and Pupil Responses

The linear discriminant analysis (Wilks-lambda criterion) demonstrated that the results of the two binocular disparity vergence and the pupillary light response tests are sufficient to classify individual subjects with high accuracy as control, acute mTBI, or Havana affected (**Table 3**). The data used in this analysis expressed the pupil responses as $mm^2/^\circ$. The canonical discriminant function for this three-way classification (**Table 4**) identified two classifier dimensions that produced a remarkable 91.8% correct rate overall, with a one-out cross-validation correct classification rate of 81.6%. Most notably, there were no classification errors between the Havana affected and the acute mTBI subjects. The three-way group separation remained at 89.8% correct overall (with no cross-classification errors between the mTBI and the Havana affected groups) when the variables with a significant age relationship were adjusted to a value for a standard age of 33.3939 years based upon estimated linear relationships in the control group.

The separation of the subject groups by the discriminant scores, across ages from 20 to 60 years, is shown in **Figures 5A–D**. The basic separation is shown for the scores in **Figure 5B**. **Figures 5C,D** show that the discriminant dimension scores were uncorrelated with the age of the subjects. Dimension 1 produced scores centered around zero for the control subjects, negative scores for the acute mTBI group, and positive scores for the Havana affected individuals (**Figure 5B**) across the entire age range of the subjects (**Figure 5C**). Dimension 2 showed lower scores for either the Havana affected or the acute mTBI group (**Figures 5B,D**). Thus, the distinctive group effects were consistent for the disparity step and the disparity pursuit tests.

DISCUSSION

In the time period since these symptom patterns were reported initially among the Havana diplomatic community, there has been a great deal of concern regarding the characterization of symptoms affecting the documented cases as well as the extent of the phenomenon in other populations at risk and in the general public. Dozens of individuals, both inside and outside the diplomatic community, have come forward with purported symptoms and, in the vast majority of cases, they have been diagnosed as not having a history and symptoms consistent with the group that we have seen from the Havana diplomatic community. We have termed this presentation as "worried well." This fact alone, as well as the potential ongoing threat to diplomatic and other "forward" deployed assets (who face myriad other threats as part of their daily work), creates a critical need for standardized, accurate diagnostic criteria.

As we have discussed in our initial publication (2), this study is limited by being a retrospective analysis of the data obtained on this group of individuals in which only medically necessary information could be collected. In addition, the study is limited by a small sample size. Nevertheless, this patient population represents the *only* opportunity to report the presenting symptoms in any population seen acutely, without the influence of outside attention or a "pre-knowledge" of symptomatic complaints. Knowledge of the unbiased presenting symptom patterns is important since new cases as well as many cases of the worried well (worried but unaffected individuals) have been reported around the globe.

The current paper presents objective clinical findings that help to distinguish the truly affected individuals from normal subjects and from a cohort with acute mTBI. These metrics effectively classify these individuals from young adulthood through their early 60 s (the age range of our exposed subjects; see **Figure 5**), with no cross-classification errors between the Havana affected subjects and the acute mTBI subjects. We suggest that pupillary light reflex and binocular disparity vergence tests can be utilized to produce sensitive and selective measures that, paired with otolith tests (subjective visual vertical and vestibular-evoked myogenic potentials), identify symptomatic Havana-type exposures objectively on the basis of clinical features. These tests are ready for operational use to help distinguish the "worried well" and the symptomatic disorders with other potential causes.

To our knowledge, this report is the first demonstration of the potential diagnostic utility of a quantitative analysis of binocular disparity-driven eye and pupil movements. Although these movements are highly consistent in control subjects (1), the neurologic significance of the differences that we observed has yet to be probed. Hence, the features that distinguish the acute mTBI and the Havana Affected subjects from the control sample need to be viewed as objective, empirical "markers." One feature of interest is that the rapid step and the slower smooth pursuit (0.1 Hz) binocular disparity tasks showed consistent results across the different subject groups. For example, the subjects with acute mTBI had lower magnitude vergence eye movements in either task than the control or the Havana affected subjects. The Havana affected subjects, on the other hand, had smaller baseline pupil areas than the control subjects for light reflex testing and during binocular disparity tests, associated with larger pupil changes per degree of vergence when data were normalized to the pupil area range.

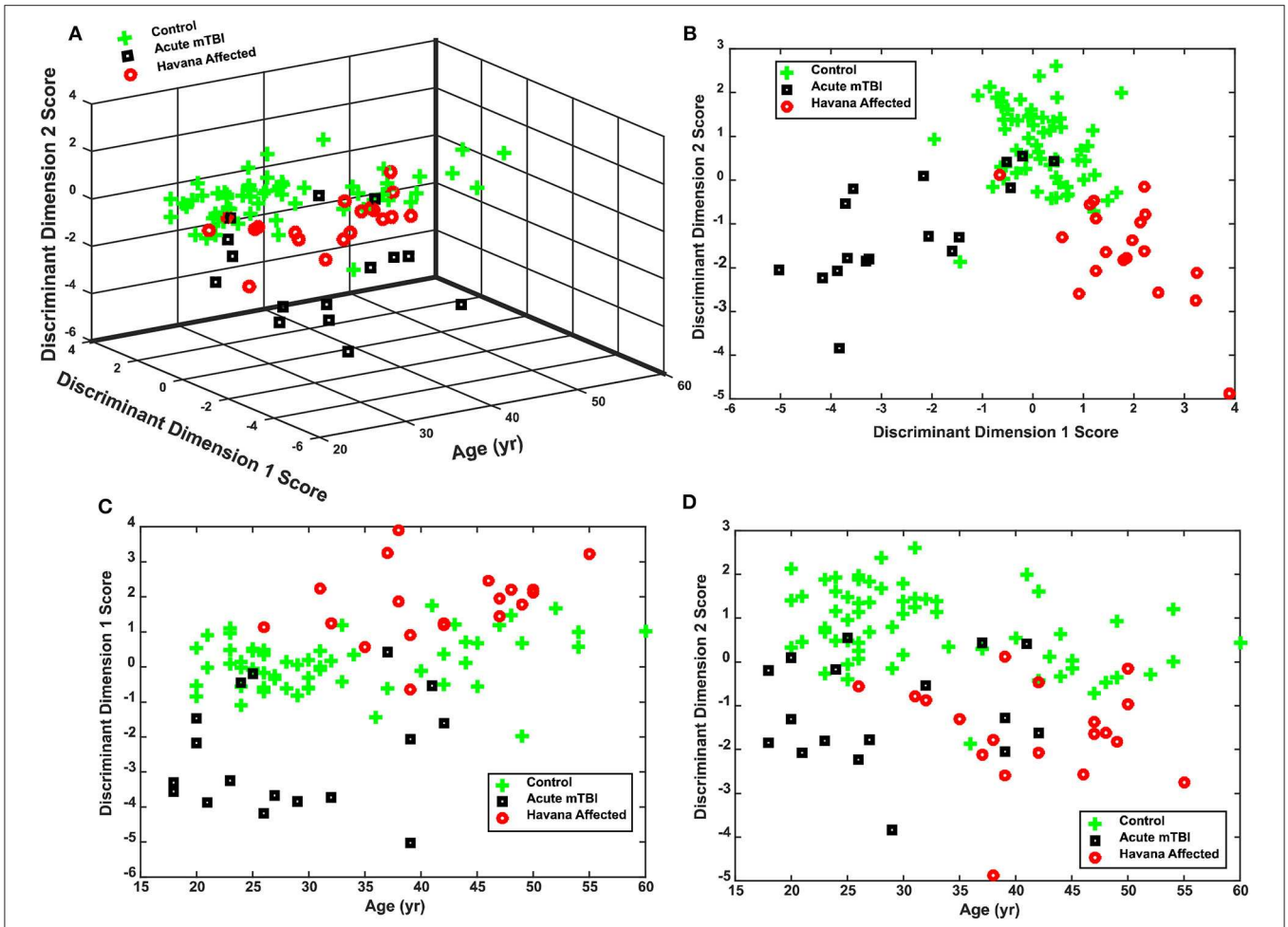

FIGURE 5 | Performance of discriminant function for classifying control, acute mild traumatic brain injury (mTBI), and Havana affected subjects. **(A)** Three-dimensional plot of the distribution of individual discriminant function scores for subjects as a function of age at time of testing. Note that the group separation does not vary with age. **(B)** Plot of the relationship between the two discriminant dimensions, collapsed across subject ages. **(C)** Separation of acute mTBI, control, and Havana affected subject by discriminant dimension 1 across ages. **(D)** Separation of acute mTBI, control, and Havana affected subject by discriminant dimension 2 across ages.

Diagnosis of convergence insufficiency (e.g., in mTBI) is typically documented by (1) a minimum near point of convergence >6 cm from the face, (2) greater exodeviation for near objects than far objects, and (3) a positive fusional vergence during a prism test. They assess the final behavior of fusion on static targets. The measures utilized in this study assess the dynamic behavior of the eyes and the pupil during the responses to binocular disparity. The acute mTBI subjects showed a distinct pattern of changes in both binocular disparity tasks. Specifically, the magnitude of the eye movements was depressed significantly and symmetrically in both converging and diverging directions, accompanied by an effect on the magnitude of pupil responses (per degree vergence) for both constriction and dilation in the disparity step task and only dilation in the disparity pursuit task. These findings indicate that the amplitudes of the convergence movements were reduced significantly in the subjects with acute mTBI relative to the control subjects. For the step task, the magnitude was less than half the control value, which would be consistent with an apparent increase in the distance of the near point of convergence (relative to the subject's head). These dynamic movement findings are likely to be predominantly a supranuclear oculomotor control phenomenon that is related to generating the parallel drive to the extraocular muscles and the pupil controller (14).

Because the etiology of the consistent patterns of findings in these individuals is unknown, it is important to also consider the possibility of functional (or psychogenic) disease. Stated bluntly, one entertains a psychogenic or functional diagnosis after excluding known organic explanations. The appearance and the diagnosis of changes in pupillary size and reactivity are among the five psychogenic patterns that are discussed in neuro-ophthalmologic literature (15–19). However, it is noteworthy that the pattern of oculomotor and otologic findings in this cluster of individuals has no precedent in the "psychogenic" literature. Further, three arguments suggest that it is premature to invoke a functional etiology. Firstly, the new eye movement findings

are sufficiently distinctive to reliably classify these individuals, control subjects, and subjects with acute mTBI with high accuracy (>91% by discriminant analysis). Secondly, the affected individuals reported perceptions that coincided with symptom onset. Thirdly, the findings are not inconsistent with either peripheral effects on the inner ear and eye or accompanying effects on the central nervous system (20).

The findings in this study are limited by the retrospective design, low subject numbers, and concerns about how to generalize the data beyond the Havana diplomatic community. However, despite these limitations and the absence of a detailed neuro-ophthalmologic consultation and exam, it remains uncertain whether the changes in pupil responses during the binocular disparity vergence tasks reflect direct ocular effects, effects on visual pathways, or adaptive responses to perturbations yet to be identified. Because the binocular disparity stimuli were predictable and relatively brief, one cannot exclude the possibility of a contribution of an impaired executive function to performance on these tasks, given the elevated prevalence of abnormal antisaccade task error rates in both subjects with acute mTBI (21) and the Havana affected cohort (2) Randomized disparity testing may be helpful in resolving the latter issue in the future. Nevertheless, our data demonstrate that the behavior of the Havana affected subjects in these tasks differed markedly from the convergence eye and the pupil coordination pattern in the acute mTBI subjects. These differences in objective performance need to be considered in the management of individuals showing features of the Havana affected group. For example, traditional mTBI treatment approaches that target convergence training may not be effective in this distinct patient population.

CONCLUSION

In late 2016, diplomats in Havana, Cuba, began presenting with a unique symptom complex after perceiving a strange noise and/or feeling a pressure field in their domicile. There have been previous reports on both the initial as well as the longer-term findings in this population. This is the first report that examines the function of these individuals on a test that examined binocular disparity-driven eye and pupil movements during the acute time period after exposure. The patterns of response in these individuals are markedly different than those seen in a group of individuals with usual acute mild traumatic brain injury and from controls with no injury. The results from these tests permitted an objective discrimination of the groups with >91% accuracy and no confusion between the Havana subjects and the subjects with acute mild traumatic brain injury. This pattern difference may be a useful screen for individuals who report a similar exposure pattern. Furthermore, their distinctive presentation may help guide in treatment decisions to address the mechanisms that contribute to their unusual symptom complexes. At the current time, however, this remains an empirical observation and more work is needed to study the findings.

DATA AVAILABILITY STATEMENT

The datasets generated for this study are available on request to the corresponding author. Q13

ETHICS STATEMENT

Q8

The studies involving human participants were reviewed and approved by The Institutional Review Boards (IRBs) at the University of Miami and Madigan Army Medical Center approved the prospective studies of control subjects and subjects with mTBI. The IRB at the the University of Miami approved the retrospective study of clinical data from the Havana Affected cohort. The University of Pittsburgh IRB approved the analysis of de-identified data from all groups. The patients/participants provided their written informed consent to participate in this study.

AUTHOR CONTRIBUTIONS

CB, MS, BL and MH contributed to the conception and design of the study and contributed to manuscript revision. CB performed the data analysis and wrote the first draft of the manuscript. CB, BL, and MH, wrote sections of the manuscript. AK contributed to device design and modifications and to technical aspects of manuscript preparation. All authors read and approved the submitted version. Q14

FUNDING

The analysis was supported by the Office of Naval Research (Grant No. 00014-18-1-2157). Q7

REFERENCES

1. Balaban CD, Kiderman A, Szczupak M, Ashmore RC, Hoffer ME. Patterns of pupillary activity during binocular disparity resolution. *Front Neurol Neuro-Ophthalmol.* (2018) 9:990. doi: 10.3389/fneur.2018.00990
2. Hoffer ME, Levin BE, Snapp H, Buskirk J, Balaban CD. Acute findings in an acquired neurosensory dysfunction. *Laryngoscope Investig Otolaryngol.* (2018) 4:124–31. doi: 10.1002/lio2.231
3. Swanson R, Hampton S, Green-Mckenzie J, Diaz-Arrastia R, Sean, MG, Verma R, et al. Neurological manifestations among US government personnel reporting directional sudible and sensory phenomena in Havana, Cuba. *JAMA*. (2018) 319:1125–33. doi: 10.1001/jama.2018.1742
4. Alvarez TL, Kim ET, Vicci VR, Dhar SK, Biswal BB, Barrett AM. Concurrent visual dysfunctions in convergence insufficiency with traumatic brain injury. *Optom Vis Sci.* (2012) 89:1740–51. doi: 10.1097/OPX.0b013e3182772dce
5. Mucha A, Collins MW, Elbin RJ, Furman JM, Troutman-Enseki C, De Wolf RM, et al. A brief vestibular/ocular motor screening (VOMS) assessment to evaluate concussions: preliminary findings. *Am J Sports Med.* (2014) 42:2479–86. doi: 10.1177/0363546514543775
6. Pearce KL, Sufrinko A, Lau BC, Henry L, Collins MW, Kontos AP. Near point of convergence after a sport-related concussion: measurement reliability and

relationship to neurocognitive imapairment and symptoms. *Am J Sports Med*. (2015) 43:3055–61. doi: 10.1177/0363546515606430
7. Ciuffreda KJ, Joshi NR, Truong JQ. Understanding the effects of mild traumatic brain injury on the pupillary light reflex. *Concussion*. (2017) 2:CNC36. doi: 10.2217/cnc-2016-0029
8. Sun F, Krenz WC, Stark LW. A systems model for pupil size effect. *I Transient data Biol Cybern*. (1983) 48:101–8. doi: 10.1007/BF00344393
9. Maxwell J, Tong J, Schor CM. The first and second order dynamics of accommodative convergence and disparity vergence. *Vision Res*. (2010) 50:1728–37. doi: 10.1016/j.visres.2010.05.029
10. Stark L, Sherman PM. A servoanalytic study of the consensual pupil reflex to light. *J Neurophysiol*. (1957) 20:17–26. doi: 10.1152/jn.1957.20.1.17
11. Sun F, Tauchi P, Stark L. Dynamic pupillary response controlled by the pupil size effect. *Exp Neurol*. (1983) 82:313–24. doi: 10.1016/0014-4886(83)90404-1
12. Krenz WC, Stark L. Systems model for pupil size effect. *II Feedback model Biol Cybern*. (1985) 51:391–7. doi: 10.1007/BF00350779
13. Privitera CM, Stark LW. A binocular pupil model for simulation of relative afferent pupil defects and the swinging flashlight test. *Biol Cybern*. (2006) 94:215–24. doi: 10.1007/s00422-005-0042-8
14. Mcdougal DH, Gamlin PDR. Autonomic control of the eye. *Compr Physiol*. (2015) 5:439–73. doi: 10.1002/cphy.c140014
15. Griffin JH, Wray SH, Anderson DP. Misdiagnosis of spasm of the near reflex. *Neurology*. (1976) 26:1018–20. doi: 10.1212/WNL.26.11.1018
16. Keane JR. Neuro-ophthalmic signs and symptoms of hysteria. *Neurology*. (1982) 32:757–62. doi: 10.1212/WNL.32.7.757
17. Weller M, Wiedemann P. Hysterical symptoms in ophthalmology. *Doc Ophthalmologica*. (1989) 73:1–33. doi: 10.1007/BF00174124
18. Newman NJ. Neuro-ophthalmology and psychiatry. *Gen Hosp Psychiatry*. (1993) 15:102–14. doi: 10.1016/0163-8343(93)90106-X
19. Miller NR. "Functional neuro-ophthalmology," in Kennard C, Leigh RJ, editors. *Handbook of Clinical Neurology*. New York, NY: Elsevier (2011). p. 493–513. doi: 10.1016/B978-0-444-52903-9.00024-8
20. Verma R, Swanson RL, Parker D, Ismaeli AAO, Shinohara RT, Alappatt JA, et al. (2019). Neruoimaging findings in US government personnel with possible exposure to directional phenomena in Havana, Cuba. *JAMA*. 322:336–47. doi: 10.1001/jama.2019.9269
21. Balaban CD, Hoffer ME, Szczupak M, Snapp H, Crawford J, Murphy S, et al. Oculomotor, vestibular, and reaction time tests in mild traumatic brain injury. *PLoS ONE*. (2016) 11:e162168. doi: 10.1371/journal.pone.0162168
22. Stevens SS. Issues in psychophysical measurement. *Psychol Rev*. (1971) 78:426–50. doi: 10.1037/h0031324
23. Stevens SS. Neural events and the psychophyxical law. *Science*. (1971) 170:1043–50. doi: 10.1126/science.170.3962.1043
24. Suzuki R, Yoshino H, Kobayashi S. Different time courses of bovine iris sphincter and dilator muscles after stimulation. *Ophthalmic Res*. (1987) 19:344–50. doi: 10.1159/000265519

Conflict of Interest: The authors declare that the research was conducted in the absence of any commercial or financial relationships that could be construed as a potential conflict of interest.

The reviewer, TA, declared a past collaboration with one of the authors, MH, to the handling Editor.

Copyright © 2020 Balaban, Szczupak, Kiderman, Levin and Hoffer. This is an open-access article distributed under the terms of the Creative Commons Attribution License (CC BY). The use, distribution or reproduction in other forums is permitted, provided the original author(s) and the copyright owner(s) are credited and that the original publication in this journal is cited, in accordance with accepted academic practice. No use, distribution or reproduction is permitted which does not comply with these terms.

APPENDIX

The model for analysis of the pupillary light responses, based upon the work of Stark and collaborators (8, 10–13), is summarized in **Figure 1**. The global luminance was transformed through a power function, where *b* is a fractional exponent that mimics the neural and the perceptual encoding of intensity (22, 23); initial values for model estimation procedures (below) were set by linear regression estimation of the relationship between the logarithms of the depth of each pupillary response and the logarithm of the stimulus intensity for that response. The luminance signals were then processed in parallel by a high-pass mechanism with transfer function $\frac{K_{lh}\ s}{0.085s+1}$ and a low-pass mechanism with transfer function $\frac{K_{ll}}{0.15s+1}$ (where "s" is a complex variable for the Laplace representation of the transfer function). The sum of these signals drives the iris musculature, with faster dynamics and a shorter delay for the sphincter muscle ($\frac{K_s e^{-0.2s}}{0.35s+1}$)than the dilator muscle ($\frac{K_d e^{-0.5s}}{3.5s+1}$). The difference in the dynamic properties of these muscle is based upon published findings from bovine muscle (24). Non-linear least squares regression ("lsqnonlin.m" function in MATLAB) was used to estimate the power function and the gain parameters from experimental data. The models were fitted initially for each eye. Since there was no significant difference between the left and the right pupil responses for these binocular stimuli, the responses were then averaged. The parameter estimates below are from the averaged data.

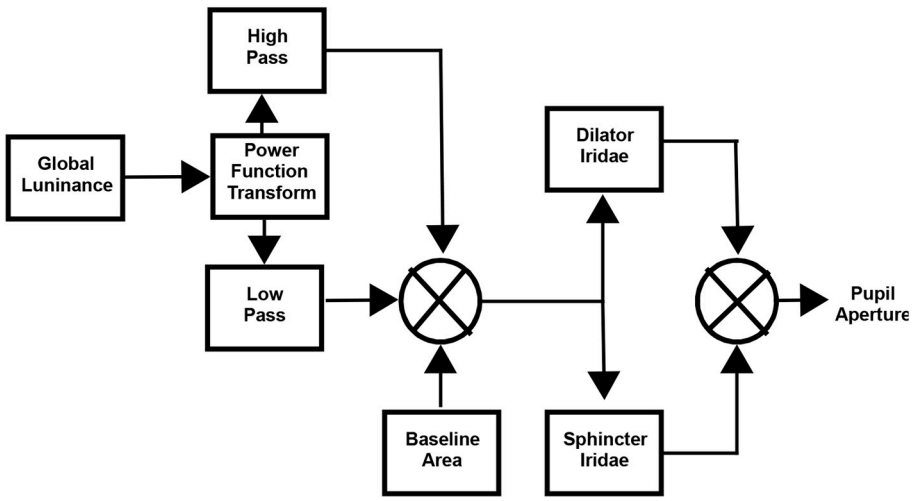

FIGURE A1 | Schematic diagram of the model for dynamic analysis of pupillary light response data. This model is a lumped representation of the processes described in a series of papers from the Stark laboratory, spanning several decades (8, 10–13).

Proceedings of the ASME 2020
International Mechanical Engineering Congress and Exposition
IMECE2020
November 16-19, 2020, Portland, OR, USA

DRAFT **IMECE2020-24213**

ULTRASONIC ACOUSTIC HETERODYNE TRANSMISSION INTO THE HUMAN AUDITORY AND VESTIBULAR SYSTEMS

Christopher M. Dumm[1], Anna C. Hiers[1], Jeffrey S. Vipperman[1,2], George E. Klinzing[3], Carey D. Balaban[4]
University of Pittsburgh
Pittsburgh, PA

ABSTRACT

It is well-known that airborne sound induces vibration of the eardrum, the coupled middle ear bones, and the inner ear. Sound transmission to the inner ear is attenuated by damage or dysfunction in the eardrum or ossicular chain. Corrective devices often use contact shakers to directly vibrate the temporal bone of the skull, delivering sound. We investigate an alternative, noncontact method of sound transmission that uses ultrasonic signals to transmit sound into the auditory and vestibular systems. Minimal literature exists describing ultrasonic hearing, largely due to attenuation of air-conducted frequencies above 20 kHz. High-amplitude airborne sound incident upon the skull can induce temporal bone system vibrations along an unconventional structural path. Finite-element-based acoustic modeling of the auditory and vestibular anatomy reveals resonant behavior in structural components of the middle and inner ear at ultrasonic frequencies. These "built-in sound amplifiers" can be leveraged to compensate for impedance mismatches experienced in airborne ultrasound transmission. By heterodyning (amplitude modulating) a targeted ultrasonic carrier signal with an audio signal, the nonlinearities of acoustic propagation and the auditory and vestibular sense organs allow interpretation of heterodyne signals. These techniques provide a foundation to improve a wide variety of communication equipment, including hearing aids, without interfering with balance sensations.

Keywords: hearing, cochlea, ultrasound, modal analysis, finite element model, heterodyne

1. INTRODUCTION

The classical air-conduction hearing path is the most common description of how sound enters the external ear and is eventually transduced to neuronal signals that are interpreted by the brain. This description is sufficient for human hearing at sound frequencies between approximately 20 Hz and 20 kHz. Outside of this range, the frequency sensitivity of the organ of Corti limits transduction of physical vibration from sound into neural signals. While exposure to ultrasonic sound (with frequency above 20 kHz) can be perceived by humans when delivered at high amplitude, the mechanism of ultrasound transduction and the structural-acoustic behavior of the anatomical system is largely unknown.

This work is intended to elucidate a candidate mechanism for delivery of ultrasonic sound into the human auditory and vestibular systems. We approach the topic from a structural-acoustic perspective, beginning with a review of the anatomy of the temporal bone of the skull, which houses the eardrum, transfer mechanisms of the middle ear, and the sense organs of the inner ear. Anatomical review leads naturally to first-principles assessment of these structures as potential acoustic resonators. More advanced computational analysis is utilized to assess the complex, interconnected geometries of the middle and inner ear spaces. We subsequently discuss how so-called acoustic heterodyne signals can be designed to strategically target the resonant acoustic structures, enabling noncontact, discreet sound transmission into the auditory and vestibular systems. Finally, we discuss applications of this technique and work required to further assess the feasibility of these techniques.

[1] Department of Mechanical Engineering and Materials Science, University of Pittsburgh, Pittsburgh, PA, USA
[2] Contact author: jsv@pitt.edu
[3] Department of Chemical and Petroleum Engineering, University of Pittsburgh
[4] Department of Otolaryngology, University of Pittsburgh

 © 2020 by ASME

2. ANATOMICAL OVERVIEW

Before discussing behavior of the auditory and vestibular systems at ultrasonic frequencies, we will review the anatomy and function of the "classical" air-conduction hearing path. Familiarity with these structures enables discussion of how other anatomical features of the temporal bone are structurally coupled with the hearing and sense organs, and leads naturally to analysis of key features of the middle ear, inner ear, and temporal bone as a system sensitive to high-frequency vibration.

2.1 The tympanic membrane and ossicles

Upon entering the external ear canal, sound impinges upon the soft-tissue tympanic membrane (eardrum), which serves as the boundary between air in the environment and the enclosed, air-containing tympanic cavity, or middle ear, depicted in detail in Figure 1. The three small bones of the middle ear (the *ossicles*) form a mechanical linkage between eardrum and the hearing organs in the fluid-filled inner ear spaces. For reasons that will shortly become clear, we note the depiction of the soft tissue oval window at the stapedial footplate as the site where tympanic membrane vibrations drive sound into the inner ear, and the similar soft tissue round window as an undriven port coupling middle and inner ear spaces.

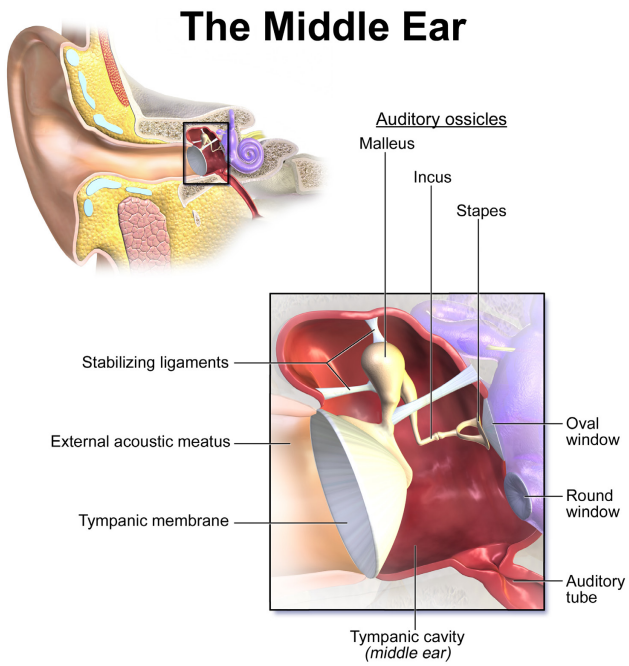

FIGURE 1: ANATOMY OF THE MIDDLE EAR [1]

2.2 The inner ear

Hearing and sense organs are located within the inner ear spaces (colloquially, the "*labyrinth*" due to its complex structure) medially adjacent to the middle ear cavity, shown in Figure 2. Like the middle ear cavity, the inner ear spaces are enclosed within the temporal bone of the skull, and specifically are surrounded by compact (*cortical*) bone, which has different material properties than vascularized, marrow-containing cortical (*trabecular*) bone.

Unlike the middle ear cavity, the inner ear spaces are filled not with air, but with fluids known as *perilymph* and *endolymph*. The depiction of the "coaxial" inner ear structure in Figure 2 distinguishes bony and membranous regions of the labyrinth. These regions' names are "structural guides" that refer to exterior cross-sectional boundaries. A thin membrane encloses the roughly circular cross-section of membranous labyrinth spaces, and the annular bony labyrinth space cross-sections are bounded by compact bone on the outer boundary and by the aforementioned membrane on the inner boundary. The bony and membranous labyrinths contain perilymph and endolymph, respectively, which have distinct ionic content and chemically facilitate the sensing processes of the auditory and vestibular sense organs.

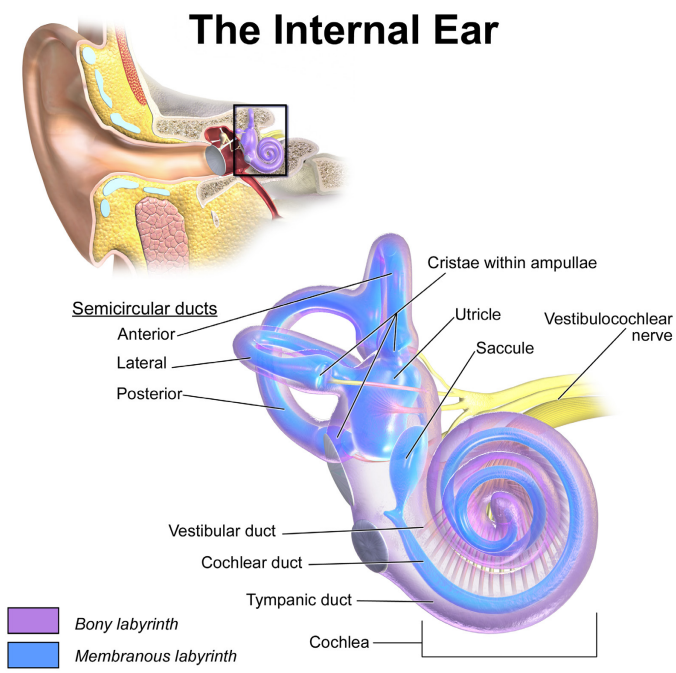

FIGURE 2: ANATOMY OF THE INNER EAR [1]

Inner ear descriptions typically divide the structure into three separate regions: the *cochlea* (the sound transducer); the semicircular canals (or ducts), which contain angular acceleration sensors for skull motions within their ampullae; and the central vestibule, which contains the *utricle* and *saccule* organs. Both the utricle and saccule are sensitive to linear acceleration and gravitational forces. While detailed microanatomical review is not required for the scope of our discussion, it is important to understand that each vestibular sense organ (utricle, saccule, and a *crista ampullaris* in each of the three semicircular canal ampullae) comprises a biological seismic mass that contributes to the actuation of innervated receptor hair cells, generating nervous system signals.

2.3 Cochlea

The fluid compartments of the hearing organ (the cochlea) are physically coupled to the vestibular sense organs via the

© 2020 by ASME

vestibule. A simple functional description of the cochlea is aided by Figure 3, which shows a schematic view of the "unwrapped" cochlea. While cochlear microanatomy is far more nuanced than described here, it suffices for our purposes to treat the cochlea as two flattened tubes sharing a common membrane, known as the *basilar membrane*. The basilar membrane is coupled to innervated hair cell sensors which transduce basilar membrane vibrations into nervous system signals. All other surfaces of the tubes (except for the vestibule and round window connections) are bounded by compact bone.

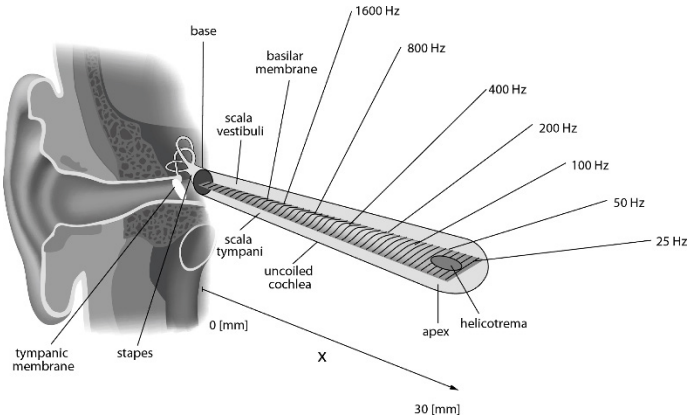

FIGURE 3: "UNWRAPPED" COCHLEA GEOMETRY WITH APPROXIMATE FREQUENCY MAPPING [2]

At the cochlear apex (the end most distal from the vestibule), the *helicotrema* is a region of perilymph continuity between the *scala vestibuli* and the *scala tympani*. In our previous discussion of Figure 2, we noted the presence of the ossicle-connected oval window as well as the nearby round window. The oval window is located on the vestibule, very close to the point where the scala vestibuli begins to enter the spiral cochlear structure. Tympanic membrane vibrations excite the ossicles and subsequently the round window, launching sound into the perilymph of the scala vestibuli. An outgoing pressure wave in the fluid travels down the length of the scala vestibuli, through the helicotrema, and back along the length of the scala tympani before reaching the round window. Because lymph is an incompressible fluid, the round window displaces inward and outward in response to the driving oval window's vibrations, maintaining system static pressure. The difference in phase between traveling pressure waves in the scala vestibuli and scala tympani generates pressure differentials across the basilar membrane, resulting in basilar membrane vibration that varies as a function of position. As Figure 3 identifies, traveling waves moving along the length of the cochlea effectively generate frequency-specific regions where maximal basilar membrane displacement is observed, leading to the commonly-cited interpretation of the basilar membrane as a physical Fourier analyzer that essentially implements a series of simultaneous narrowband filters. While this interpretation is now widely recognized as imprecise [3], the general physical reality that low-frequency hearing relies heavily on hair cell activation near the helicotrema and that high-frequency perception is localized to the cochlear base is useful for our discussion.

2.4 Impedance matching and hearing correction

The ossicular chain serves a critical function as an impedance matching network. If sound in the environment directly actuated the oval window, an acoustical impedance mismatch between perilymph and air of approximately 3500:1 would be present, leading to very low transmission into the inner ear. Instead, the ossicles' mechanical coupling between the tympanic membrane and oval window results in an overall higher sound pressure level in the cochlea compared to the stimuli in the ear canal [4]. It follows naturally that dysfunction in the ossicular chain results in lower transmission of sound to the cochlea.

While conventional hearing aids that amplify sound in the ear canal can be used to address air-conductive hearing loss, an alternative management strategy is the use of a bone-conduction hearing aid, which uses a mechanical vibrator pressed against the skin to excite the temporal bone. Vibration of the bony walls of the labyrinth constitutes a "base motion" vibration scenario for the basilar membrane, inducing membrane vibration and the generation of electrical signals by the embedded hair cell transducers. This arrangement presents a more favorable impedance mismatch for conduction from bone into lymph at approximately 4:1, although an additional skin-to-bone impedance mismatch at approximately 1:5 and the damping of soft tissues must be overcome, requiring relatively high vibratory amplitudes. These transducers are frequently held in place over the skin with eyeglasses or compression bands, which may allow motion and imperfect contact. Other mounting options include the surgical implantation of an anchor into the temporal bone, which minimizes the skin-bone impedance mismatch but introduces surgical risk.

2.5 Mastoid air spaces

Classical descriptions of the air-conductive and bone-conductive hearing paths omit an anatomical feature we find important in analysis of the temporal bone as a coupled system. The middle and inner ear are specifically housed within the petrous part of the temporal bone. As indicated on the left human temporal bone shown in Figure 4, the petrous part is a dense protrusion extending medial and anterior from the curvature of the external skull (the squamous part of the temporal bone).

© 2020 by ASME

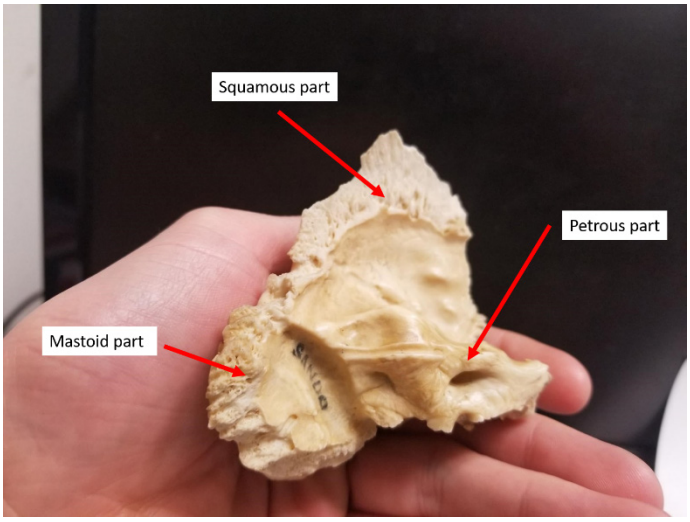

FIGURE 4: LEFT TEMPORAL BONE, HUMAN

Posterior to the squamous and petrous parts, able to be felt by hand immediately behind the external ear is the thumb-sized, protruding mastoid part of the temporal bone. The mastoid has an unusual, "pneumatized" internal structure, illustrated in Figure 5, which consists of a large number of complex air-filled cells that are demarcated by thin (order of 100µm) laminae of compact bone. Cells are not sealed: air in one cell is contiguous with others through the tympanic antrum. The shared air space extends up to (and is contiguous with) the middle ear cavity, i.e. acoustically, vibration in the middle ear air space propagates into the mastoid, and vice versa. Figure 5 also shows the close proximity of the semicircular canals (*Prominence of lateral semicircular canal*) to a section of the air space (*Tympanic antrum*). These structures are physically separated by a thin (<1 mm) compact bone layer. We will explore the acoustic behavior of these interconnected structures in a subsequent section.

3. ULTRASONIC ANATOMICAL BEHAVIOR

The human auditory system is widely considered only to be able to perceive sound frequencies between 20 Hz and 20 kHz. Historical studies indicate low-pass behavior of the combined middle and inner ear systems in mammals (including humans), with sound transmission roll-off in humans beginning in the 1-2 kHz range [6, 7]. Lack of human perception in higher frequency ranges has historically led to limited assessment of auditory behavior at ultrasonic frequencies. The available work in this area indicates that ultrasound delivered via bone conduction can be perceived by humans, including interpretation of speech modulated to ultrasonic frequencies [8]. With an appropriate bone-coupled transducer, human hearing thresholds for frequencies between 20 kHz-100 kHz have been measured to be on the order of 120-130 dB_{SPL} re. 1 µbar [9]. Experimenters in this area have noted the occurrence of short-term tinnitus in some subjects, which is typically attributed to the high sound amplitudes employed in the experiment. [9, 10] Some investigators attribute the discomfort and changing perceived locations of ultrasonic phenomena as an effect of bone standing wave patterns [10], but we are not aware of any investigation identifying structural-acoustic features in the temporal bone which might interact with ultrasonic vibrations.

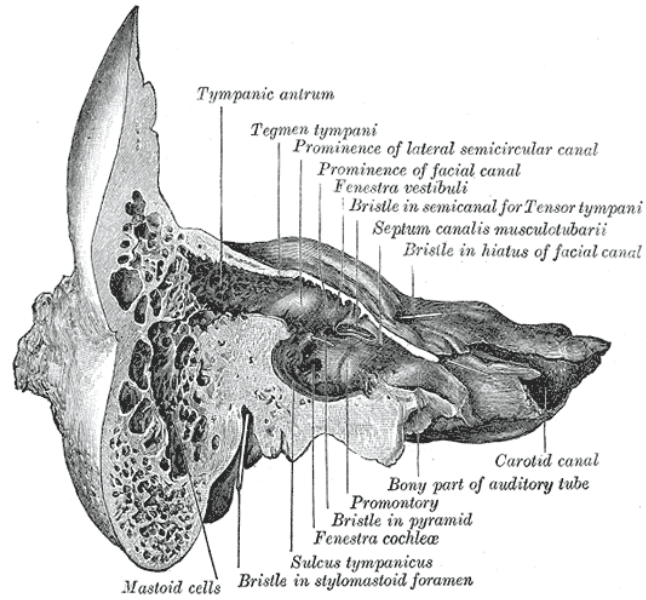

FIGURE 5: CORONAL SECTION OF TEMPORAL BONE [5]

Our review of the temporal bone in a structural-acoustic context reveals the presence of anatomical features that could act as physical ultrasonic resonators. In the inner ear, the extension of the semicircular canals and the cochlea from the central vestibule constitute acoustic ducts which could maintain various standing and traveling wave modes. A typical human inner ear fits within a 20 mm cube, with an approximate unwrapped cochlear length of 30 mm and semicircular canals on the order of 15-25 mm. Treating a semicircular canal as a 15 mm long, half-wave resonant, water-filled acoustic duct with Dirichlet boundary conditions (zero dynamic pressure at the vestibule connections), the first natural frequency is given by:

$$f_1 = \frac{c}{2L} = \frac{(1450m/s)}{2*(0.015m)} = 48.3\ kHz \qquad (1)$$

A similar treatment of the cochlea as a quarter-wave (Helmholtz) resonator (comprising two connected 30 mm pipes) bounded by a Dirichlet condition at the vestibule and a Neumann condition (zero dynamic pressure gradient) at the round window gives a first natural frequency of:

$$f_1 = \frac{c}{4L} = \frac{(1450m/s)}{4*(2*0.030m)} = 6.04\ kHz \qquad (2)$$

Naturally, these simple analyses will invariably be inaccurate due to the complex, interconnected form of the cochlea and the unmodeled physics of the basilar membrane, but they provide a simple estimate that implies the existence of high-frequency structural resonances of the system, and a basis for assessing the validity of more advanced models.

© 2020 by ASME

This modeling strategy becomes far more complex for the middle ear spaces. While the tympanic cavity itself is a relatively well-defined cavity, the connected pneumatized bone in the mastoid is highly complex. The coupled air-filled space (with longest dimension on the order of 40 mm) will likely have standing modes at relatively high frequencies. Furthermore, the small air pockets and thin "beams" of bone inside the mastoid could each constitute a high-frequency mechanical resonator. As discussed previously, vibrations generated in the mastoid can propagate into the main middle ear cavity, where they could interact with the tympanic membrane, the oval window, or the round window. Resonance of thin bone layers could also propagate directly through the temporal bone and excite other locations in the middle or inner ear.

4. FINITE-ELEMENT ACOUSTIC MODELING OF VESTIBULAR AND AUDITORY GEOMETRY

Analyzing the existence and frequency of resonant phenomena in the auditory and vestibular systems requires the use of realistic anatomical geometry and a computational modeling package. Here we discuss construction and outcomes of acoustic models of the inner ear and middle ear spaces.

4.1 The OpenEar Temporal Bone Dataset

Appropriate anatomical could be obtained by reconstruction of imagery from computed tomography (CT) scanning or microtome sections. Both types of imagery as well as 3D models were available in the open-source OpenEar library of 3D models of the human temporal bone generated by Sieber, et. al. [11, 12]. This dataset includes CT data, micro-sliced imagery, 3D reconstructions and registrations of all available images, and 3D models of the segmented data for 8 temporal bone specimens.

4.2 Inner ear finite-element acoustic model

We used finished 3D models from the "ALPHA" specimen of [12] corresponding to the inner ear geometry to create a finite-element (FE) acoustic model of the inner ear. Figure 6 shows the geometry of this model (implemented using ANSYS® Mechanical™), which incorporates the vestibule, semicircular canals, and cochlea. In order to ensure contiguous fluid space, a small spherical body was inserted at the site of the helicotrema and connected geometrically with the scala vestibuli and scala tympani bodies from [12]. The cochlea itself was represented as two fluid canals, unconnected through the basilar membrane and with a small physical gap left in the system. Similarly, the portion of the scala tympani nearest the round window was left unconnected to the vestibule, approximating the closed boundary condition of the round window. All other boundary conditions were left as a (natural) Neumann boundary condition. The material properties of water were used as an approximation for perilymph and endolymph in all volumes. An undamped eigensolver was used to solve a mesh of quadratic tetrahedral acoustic fluid elements, with mesh sizing sufficiently fine to avoid spatial aliasing. The analysis performed assumed linear acoustic material properties and physics.

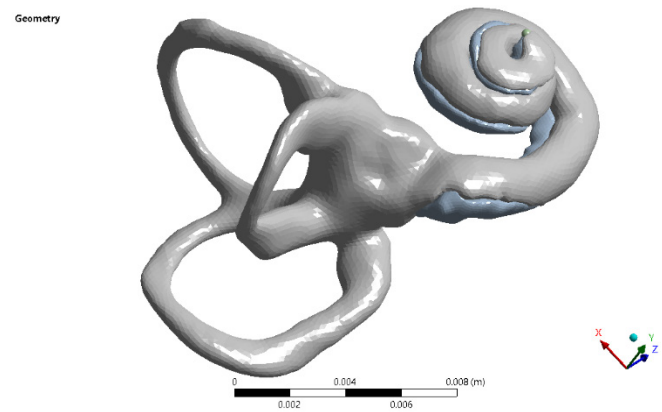

FIGURE 6: INNER EAR ACOUSTIC MODEL GEOMETRY

4.3 Inner ear modal analysis results

Modal analysis solutions (eigenvectors in acoustic pressure) from the inner ear FE model are shown in Figure 7 and Figure 8. These mode shapes correspond to the first and second vibration modes associated with the cochlear "acoustic duct" at 7.3 kHz and 20.1 kHz, respectively. These modes, as well as additional higher-frequency modes not shown here, have the characteristic quarter-wave resonator response, with high-magnitude pressure at the "closed" round window site and a relatively isobaric vestibule and semicircular canal system. We can therefore consider the theoretical first cochlear natural frequency prediction of approximately 6 kHz from the previous section to be reasonably accurate, especially since the sound-hard vestibule/semicircular canal system is not a true zero-pressure boundary condition. The second natural frequency is approximately three times the first natural frequency, further confirming the approximation of the cochlea as a quarter-wave resonator. Higher-order cochlear modes (at 32.6 kHz and 48.2 kHz, among others) were also identified by the modal analysis, indicating the potential for ultrasonic-frequency resonant waveguide behavior of the cochlea.

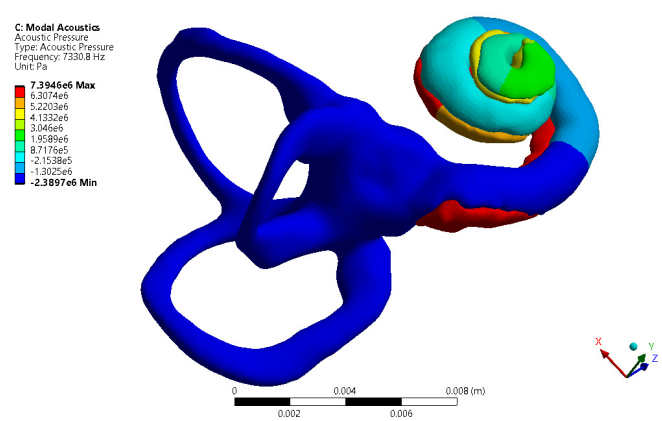

FIGURE 7: COCHLEAR ACOUSTIC DUCT MODE, 7.3 KHZ

© 2020 by ASME

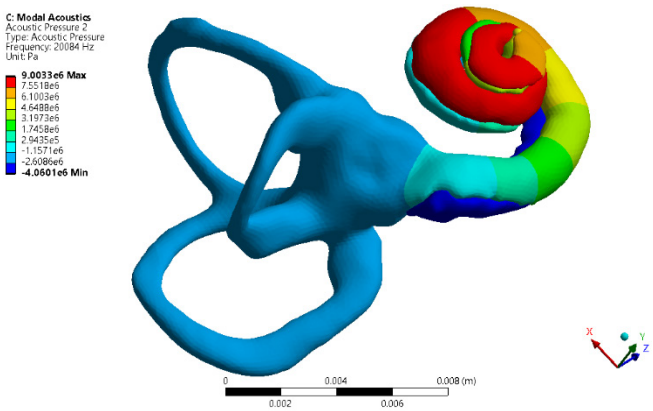

FIGURE 8: COCHLEAR ACOUSTIC DUCT MODE, 20.1 KHZ

The semicircular canals were the site of several acoustic resonant features. As theory (and practical experience with any pipe-based musical instrument) predicts, the lowest-frequency mode shape (42.8 kHz) corresponds to the longest semicircular canal (the posterior canal), shown in Figure 9. Even though a complicated connection with the superior (anterior) semicircular canal exists, this mode clearly corresponds to the mode shape of a so-called "open-open" half-wave acoustic resonator, with a high-amplitude region at the center of the duct and zero dynamic amplitude at the duct ends. Figure 10 displays a similar open-open mode at 54.9 kHz generated within the superior semicircular canal, and Figure 11 shows a more complex, higher-order mode at 77 kHz which involves both the posterior and superior semicircular canals near the crus commune.

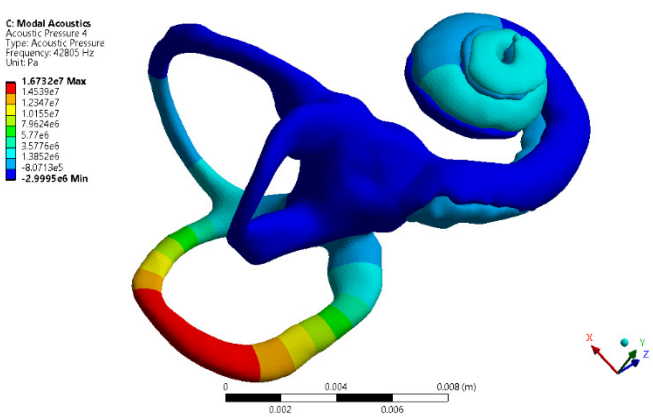

FIGURE 9: SEMICIRCULAR CANAL DUCT MODE, 42.8 KHZ

While this computational model is simplified and does not include the structural details of the semicircular canal ampullae, utricle, and saccule that generate vestibular signals, nor the cochlear microstructure that transduces sound, these results indicate the existence of ultrasonic-frequency acoustic modes in the fluid spaces of the inner ear. The mode shapes displayed here represent acoustic pressure distributions, rather than acoustic velocity of the fluid. However, regions with low acoustic amplitude typically have the greatest acoustic velocity; these regions include the sites of the semicircular canal ampullae, the saccule near the oval window (adjacent to the entrance to the cochlear scala vestibuli), and the most basal portion of the basilar membrane of the cochlea (associated with high-frequency hearing). Any purely-computational analysis of a complex anatomical structure like the inner ear is inherently speculative and eventually requires empirical validation. The rigid-walled modes discussed here do not account for the complex coupling with (and structurally-dominated modes of) the temporal bone. However, the prediction of high acoustic velocity in perilymph and endolymph near the auditory and vestibular sense organs indicates that high-frequency sound in the inner ear may be amplified by these acoustic modes. Such sound would prompt fluid motion that could activate the sense organs, generating the sensation of sound in the brain.

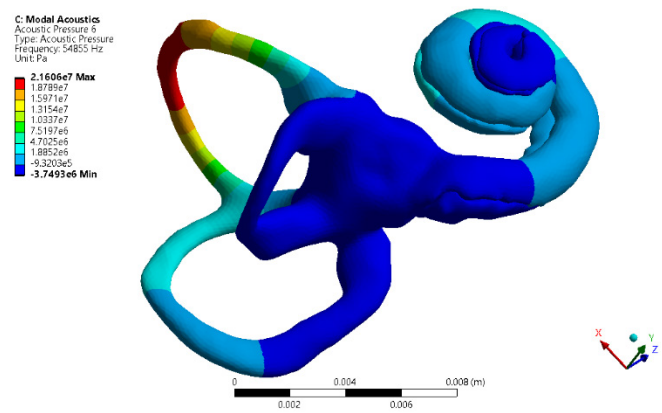

FIGURE 10: SEMICIRCULAR CANAL DUCT MODE, 54.9 KHZ

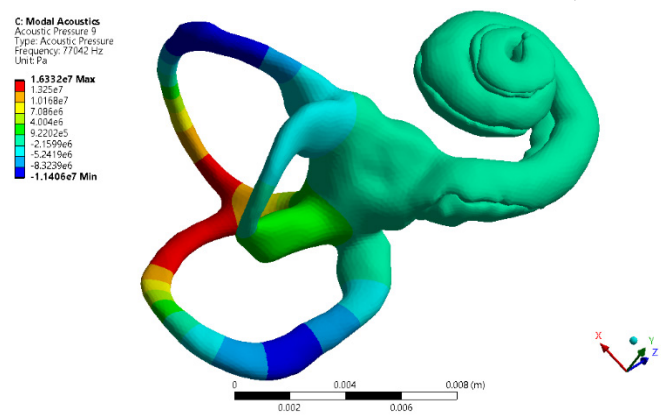

FIGURE 11: SEMICIRCULAR CANAL DUCT MODE, 77 KHZ

4.4 Middle ear finite-element acoustic model

A separate analysis of the middle ear and mastoid air spaces was conducted to identify the presence of any similar resonant features in an ultrasonic frequency range. In the closed middle ear cavity, any resonant feature would constitute a standing wave that is 3-dimensional in nature. Mechanical amplification from resonant behavior could result in high-amplitude vibration of bone or the soft tissues of the tympanic membrane, oval window, and/or round window, and projection of high-amplitude sound into the inner ear.

© 2020 by ASME

Generation of a FE model for the middle ear air space required additional processing of the data from [12] because, unlike the inner ear spaces, the middle ear air spaces were not presegmented and presented as a solid model. We used Materialise Mimics® to analyze the CT data from the "BETA" specimen of [12] and construct a solid model (shown in Figure 12) corresponding to the middle ear cavity and the mastoid antrum (the relatively open space within the center of the mastoid). To avoid excessive complexity and focus on identifying the most prominent acoustic modes of the inner ear, the smallest pneumatized cells of the mastoid were not resolved in this model. The space typically occupied by the ossicles was left as a void in the air-filled solid model structure. The same software package and mesh generation methodology used to conduct the inner ear analysis was utilized to generate the middle ear FE model, with all exterior surfaces of the computational space left in their natural (sound-hard) boundary condition.

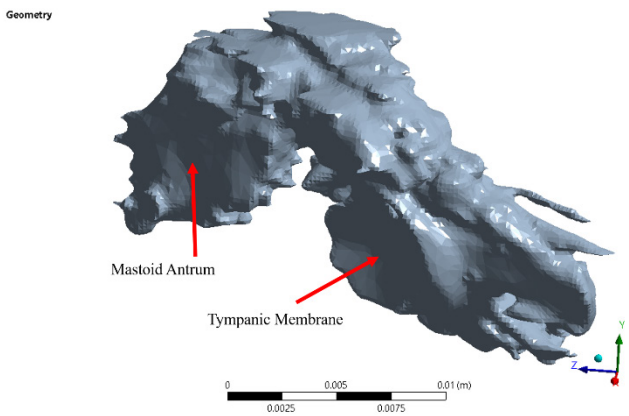

FIGURE 12: MIDDLE EAR AIR SPACE GEOMETRY, WITH TYMPANIC MEMBRANE AND MASTOID ANTRUM INDICATED

4.5 Middle ear modal analysis results

The first two natural frequencies (at 5.7 kHz and 13 kHz) and mode shapes of the middle ear space are shown in Figure 13 and Figure 14. These mode shapes correspond to the first two closed-closed "acoustic duct" modes along the long axis of the air space. Both of these modes are within the widely-accepted human hearing range, but the presence of acoustic modal nodes near the eardrum and oval/round windows (e.g. the middle of the mode shape in Figure 13) likely prevents interaction with the auditory system in normal circumstances.

Interesting higher-order modes occur at 27.5 kHz (Figure 15) and 32.5 kHz (Figure 16), where two regions along the "arch" of the air space experience high amplitudes. These modes are particularly notable because, as mentioned previously, the medial high-amplitude air regions are immediately adjacent to semicircular canals, with less than 1mm of bone separating the structures. The close physical proximity increases the probability of transfer of resonance-amplified sound into the inner ear. One additional mode at 30.5 kHz, shown in Figure 17, is transverse to the mode shown in Figure 13, and is housed entirely within the mastoid. High-amplitude resonant behavior here would likely excite the entire temporal bone, in a similar manner to a bone-conduction hearing aid.

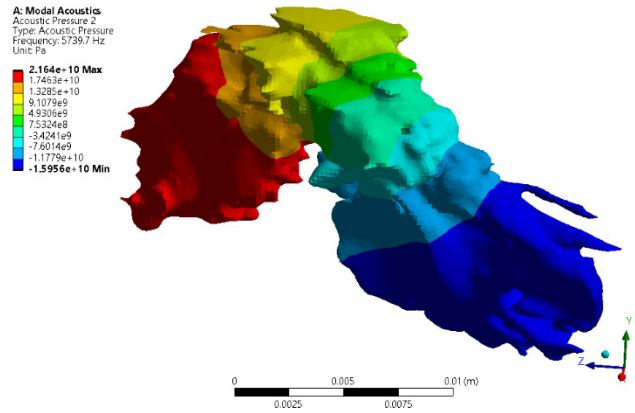

FIGURE 13: MIDDLE EAR ACOUSTIC AXIAL MODE, 5.7 KHZ

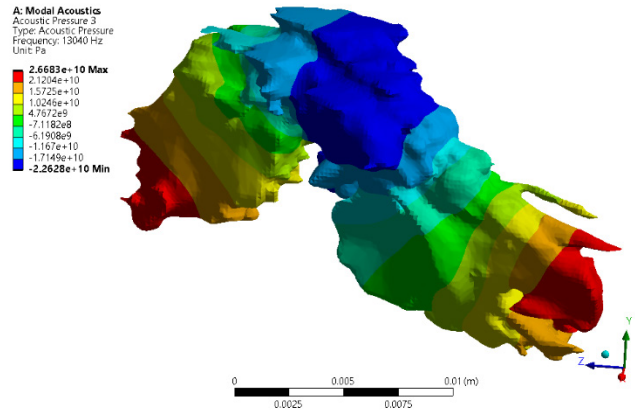

FIGURE 14: MIDDLE EAR ACOUSTIC AXIAL MODE, 13 KHZ

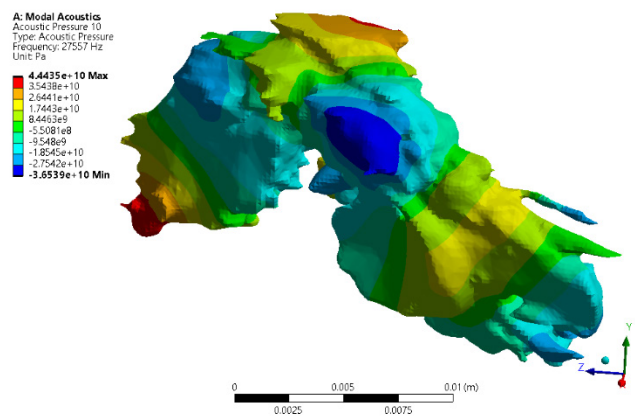

FIGURE 15: MIDDLE EAR CROSS-MODE, 27.5 KHZ

© 2020 by ASME

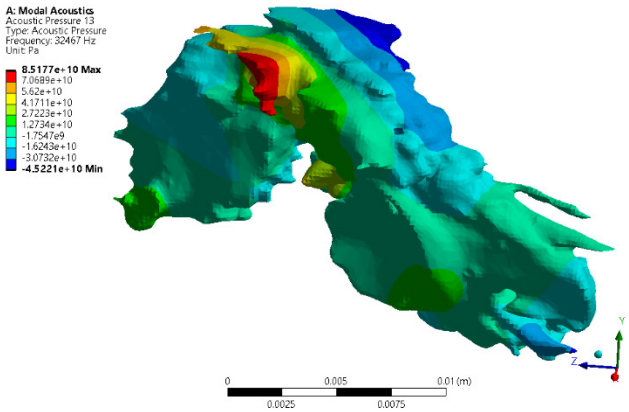

FIGURE 16: MIDDLE EAR CROSS-MODE, 32.5 KHZ

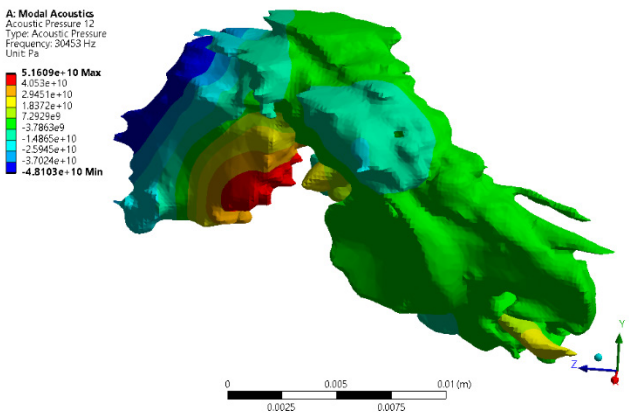

FIGURE 17: MASTOID CROSS-MODE, 30.5 KHZ

5. ACOUSTIC HETERODYNE TRANSMISSION

Resonant features of the middle ear and inner ear anatomy provide a potential pathway to transmit information into the auditory and vestibular systems with a noncontacting driver.

5.1 Ultrasonic sound projection and heterodyning

Rather than simply increasing the amplitude of a transducer to achieve ultrasound delivery, we posit that an ultrasonic signal with frequency in the neighborhood of a major resonant frequency can leverage mechanical amplification to deliver sound to the sense organs. Various systems exist which project particularly high-amplitude (e.g. 120 dB_{SPL} peak output) amplitude-modulated ultrasound to generate localized audio-frequency sound fields [13]. These systems normally rely on the weak nonlinearities of air to demodulate the ultrasound signal. Even with advanced signal preprocessing to control distortion, an audio-frequency signal with useful amplitude generated via nonlinearity is still several orders of magnitude lower in amplitude than the driving ultrasonic signal (e.g. with the device of [13], a 120 dB_{SPL} peak ultrasonic output at the measurement site resulted in audio-band amplitude of 80 dB_{SPL}).

The amplitude modulation process ("heterodyning," using Fessenden's classic term) comprises multiplication of two sinusoidal signals, typically known as an information signal and a higher-frequency carrier signal. The multiplication eliminates the original information and carrier signal frequencies, and generates an output signal with energy at two new frequencies: the sum and difference of the original carrier and information signals. In the most common application (AM radio), these new, "heterodyne" frequencies are processed in accordance with standard transmission protocols, amplified, and projected electromagnetically. A similar process can be used to generate so-called "acoustic heterodyne" signals, which can be projected acoustically by any speaker with appropriate frequency response. In the case of a 2 kHz information signal and a 40 kHz carrier signal, for example, the heterodyne frequencies would be 38 kHz and 42 kHz.

5.2 Direct acoustic heterodyne projection

With careful selection of carrier signals, acoustic heterodyne signal frequencies can be manipulated to match an anatomical resonant frequency in the middle or inner ear (e.g. the 30.5 kHz mastoid cross-mode described previously). An airborne ultrasound projector located behind the head could then transmit ultrasonic sound directly to the temporal bone at or near an anatomical resonant frequency, using mechanical amplification to compensate for impedance mismatches between air, skin, and bone. Such an approach could eliminate the advanced signal processing and high amplitudes used to ensure in-air demodulation by existing devices, and be inaudible by conventional air-conductive hearing to anyone not in the beam path. While the mechanics of ultrasonic sound perception are not entirely understood, the historical work in this area indicates a few possible explanations. One possibility is that the modulated ultrasound signals are demodulated in the fluids of the temporal bone (air and lymph) by these fluids' inherent nonlinearities, or in the known-nonlinear structure of the cochlea, and interpreted in the cochlea (in a specific region) in a manner similar to typical air-conducted sound [10, 13]. Another possibility is that some combination of nerve signals generated by the vestibular sense organs and cochlea provide sufficient information to the brain to interpret amplitude-modulated sound [8].

5.3 Applications

Unlike existing airborne ultrasonic transmitter systems that generate conventionally-audible sound to be carried along the standard air-conduction hearing path, this process of acoustic heterodyne transmission directly into the sense organs would be accessible to individuals with ossicular chain dysfunction. Transmission via inaudible ultrasound could provide a more discreet, more energy-efficient method of information transmission even for users with unimpaired hearing.

An additional possibility arising from use of this technique is the use of simultaneous heterodyne signals targeted toward specific features (e.g. the individual semicircular canals). Such a scenario would enable construction of stimuli that activate the vestibular and auditory sense organs independently or semi-independently (in control systems terminology, full controllability of each sense organ). A well-crafted stimulus may be able to accomplish sound transmission while avoiding activation of the vestibular sense organs, which are speculated to

© 2020 by ASME

be affected by ultrasonic exposure and have even been noted to cause short-duration physiological balance disruptions [13].

6. CONCLUSIONS AND FUTURE WORK

Acoustic resonant phenomena in the middle and inner ear anatomy provide a pathway to transmit vibration information into the vestibular and auditory systems without the complexity and discomfort of a contact transducer. The acoustic modeling performed in this investigation reveals that heterodyned acoustic signals may be mechanically amplified in the skull, enabling the use of smaller and lower-amplitude transmission devices.

Further assessment of this concept would likely involve computational analysis of a more advanced structural-acoustic model, including the coupling between the middle ear space, the inner ear spaces, and the temporal bone itself. Inclusion of more detailed cochlear and semicircular canal geometries would also improve the quality of predictions. Use of nonlinear physical models for all geometry could enable prediction of the extent of internal demodulation of heterodyne signals. Ultimately, physical validation will include the instrumentation of cadaveric specimens and human subjects to determine the quantitative extent of sound demodulation taking place within the middle and inner acoustic spaces, as well as the qualitative perception of sound by individuals.

ACKNOWLEDGEMENTS

Finite element analysis images used courtesy of ANSYS, Inc. This work was sponsored by the Department of the Navy, Office of Naval Research, under Grant N000014-18-1-2157. Any opinions, findings, and conclusions or recommendations expressed in this material are those of the author(s) and do not necessarily reflect the views of the Office of Naval Research or the Department of Defense.

REFERENCES

[1] Blausen.com staff (2014). “Medical gallery of Blausen Medical 2014,” accessed May 1, 2020. WikiJournal of Medicine **1** (2). DOI:10.15347/wjm/2014.010. ISSN 2002-4436. Used under the Creative Commons Attribution License 4.0: https://creativecommons.org/licenses/by/4.0/.

[2] Kern A., Heid C., Steeb W.-H., Stoop N., Stoop R., 2008, “Biophysical Parameters Modification Could Overcome Essential Hearing Gaps,” PLoS Comput Biol, 4(8): e1000161. Doi: 10.1371/journal.pcbi.1000161. Used under the Creative Commons Attribution License 4.0: https://creativecommons.org/licenses/by/4.0/.

[3] Duifhuis, H., 2012, Cochlear Mechanics: Introduction to a Time Domain Analysis of the Nonlinear Cochlea. Springer, Boston, MA. Doi: 10.1007/978-1-4419-6117-4

[4] Olson, E., 1999, “Direct Measurement of intra-cochlear pressure waves,” Nature, 402, pp. 526-529. Doi: 10.1039/990092

[5] Gray, H., 1918, “Fig. 139”, Anatomy of the Human Body, 20th ed. Bartleby.com, published May 2000, accessed May 1, 2020, https://www.bartleby.com/107/illus139 html.

[6] Kringlebotn M., Gundersen T., 1985, “Frequency characteristics of the middle ear,” J Acoust Soc Am, 77(1), pp. 159-164. Doi: 10.1121/1.392280

[7] Voss S.E., Rosowski J.J., Merchant S.N, Peake W.T, 2000, “Acoustic responses of the human middle ear,” Hear Res, 150(1-2), pp. 43-69. Doi: 10.1016/s0378-5955(00)00177-5

[8] Lenhardt M.L., Skellett R., Wang P., Clarke A.M., 1991, “Human ultrasonic speech perception,” Science, 253(5015), pp. 82-85. Doi: 10.1126/science.2063208

[9] Corso J.F., 1963, “Bone-Conduction Thresholds for Sonic and Ultrasonic Frequencies,” J Acoust Soc Am, 35, pp. 1738-1743. Doi: 10.1121/1.1918804

[10] Deatherage B.H., Jeffress L.A., Blodgett, H.C., 1954, “A Note on the Audibility of Intense Ultrasonic Sound,” J Acoust Soc Am, 26, p. 582. Doi: 10.1121/1.190379

[11] Sieber D.M., Erfurt P., John S. et al., 2019, “The OpenEar library of 3D models of the human temporal bone based on computed tomography and micro-slicing,” Sci Data, 6, 180297. Doi: 10.1038/sdata.2018.297.

[12] Sieber D.M., Erfurt P., John S. Ribero dos Santos G., Schurzig D., Sørensen M, Lenarz, T., 2019, “The OpenEar library of 3D models of the human temporal bone based on computed tomography and micro-slicing [Data set]”, Sci Data/Zenodo. Doi: 10.5281/zenodo.1473724. Used under the terms of https://creativecommons.org/licenses/by/4.0/.

[13] Pompei, F.J., 2002, “Sound From Ultrasound: The Parametric Array as an Audible Sound Source,” Ph.D. dissertation, Massachusetts Institute of Technology, Cambridge, MA.

© 2020 by ASME